





Water Resources Research®



RESEARCH ARTICLE

10.1029/2022WR032218

Quantifying Reagent Spreading by Cross-Borehole Electrical Tomography to Assess Performance of Groundwater Remediation

L. Lévy¹ , R. Thalund-Hansen² , T. Bording³, G. Fiandaca⁴, A. V. Christiansen³ , K. Rügge⁵, N. Tuxen⁶, M. Hag⁶, and P. L. Bjerg² 

Key Points:

- Reagent injection leads to a heterogeneously distributed remediation cloud, imaged by 2D cross-borehole electrical resistivity tomography (ERT) with high spatial resolution
- Chemical analyses are needed to understand which compounds affect the ERT response: Fe(diss), Ca²⁺, HCO₃⁻, and most likely solid iron
- The initial *K*-distribution, inferred from ERT/induced polarization and grain size analyses, does not explain reagent spreading after high-pressure injection

Supporting Information:

Supporting Information may be found in the online version of this article.

Correspondence to:

L. Lévy,
lea.levy@tg.lth.se

Citation:

Lévy, L., Thalund-Hansen, R., Bording, T., Fiandaca, G., Christiansen, A. V., Rügge, K., et al. (2022). Quantifying reagent spreading by cross-borehole electrical tomography to assess performance of groundwater remediation. *Water Resources Research*, 58, e2022WR032218. <https://doi.org/10.1029/2022WR032218>

Received 18 FEB 2022

Accepted 28 AUG 2022

Author Contributions:

Conceptualization: T. Bording
Data curation: L. Lévy, R. Thalund-Hansen, K. Rügge
Formal analysis: L. Lévy
Funding acquisition: P. L. Bjerg
Investigation: P. L. Bjerg
Methodology: L. Lévy, T. Bording, G. Fiandaca

¹Engineering Geology, Lund University, Lund, Sweden, ²Department of Environmental Engineering, Technical University of Denmark, Lyngby, Denmark, ³HydroGeophysics Group, Department of Geoscience, Aarhus University, Aarhus C, Denmark, ⁴Dipartimento di Scienze della Terra “A. Desio”, Università degli Studi di Milano, Milano, Italy, ⁵COWI, Parallelvej, Lyngby, Denmark, ⁶Region Hovedstaden, Hillerød, Denmark

Abstract In situ remediation of contaminated groundwater often relies on the installation of a treatment zone (TZ) degrading the contamination. Zero-valent-iron (ZVI) is a type of reagent used for this purpose. Adequate delivery of ZVI in the whole target volume is particularly challenging and requires monitoring with high spatial resolution. We present a monitoring tool for imaging the dynamic spreading of ZVI and its associated ionic cloud, using cross-borehole time-lapse electrical resistivity tomography (ERT). This tool works in urban areas and is particularly suitable for achieving the required spatial resolution at the scale of the target volume. Groundwater and sediment samples show a consistent spatial and temporal distribution of the remediation cloud with cross-borehole ERT. Yet, the 2D anomalies observed with cross-borehole ERT provide a more spatially complete and rapid image of the remediation cloud distribution than if based solely on monitoring screens. At the study site, ZVI injection leads to uneven spreading, clearly documented by cross-borehole ERT monitoring. The benefit of hydraulic conductivity (*K*) mapping by cross-borehole induced polarization (IP) to understand unexpected injection paths (upstream leakage, spreading in preferred pathways) is investigated. A 2D, IP-based, continuous, and coherent *K*-distribution is obtained that compares well with estimations by grain size analyses from the TZ. However, the IP-based *K*-field fails at predicting injection paths, suggesting the creation of pathways during the high-pressure injection of ZVI. Cross-borehole time-lapse ERT is the most promising geophysical tool for performance assessment of in situ remediation involving reagents with conductivity contrast.

1. Introduction

Industrial application of environmentally hazardous substances have led to contamination of important groundwater aquifers worldwide. Decreasing groundwater quality poses risks to human health, water and food supply, and biodiversity. In Europe, a total of 2.8 million contaminated sites was estimated in 2017 (Pérez & Eugenio, 2018), while in the US, the legal authorities had to manage up to 1.3 million contaminated sites in 2017 (U.S. Environmental Protection Agency, 2017). In Denmark, groundwater is the primary source for drinking water and >36,000 contaminated sites were registered in 2018 (Olsen et al., 2020). Source zone remediation by excavation is a typical, but expensive method that can lead to a significant carbon footprint (Søndergaard et al., 2018). In many cases, the source zone contamination depletes and creates a contamination plume in the groundwater aquifer (Fjordbøge et al., 2017; Murray et al., 2019; Steelman et al., 2020).

The development of cost-effective in situ remediation technologies, where contaminant plumes are directly treated in the groundwater, is a high priority (Ciampi et al., 2019; Ottosen et al., 2021; Verardo et al., 2021). In situ remediation methods often rely on the generation of a treatment zone (TZ), where a reactive agent is injected to intersect the contaminant plume. Examples of reactive components include strong chemical oxidants (Bording et al., 2021; Tsitonaki et al., 2010), microscale zero-valent-iron (mZVI; Xin et al., 2015) and electron donor and microbial enrichment cultures including specific degrading bacteria, e.g., *Dehalococcoides* (Scheutz et al., 2008).

Successful delivery into the subsurface is very challenging for all injection methods (Phenrat et al., 2009). Rapid assessment of reagent distribution is crucial to determine whether sufficient contact between the contaminated

© 2022. The Authors.

This is an open access article under the terms of the [Creative Commons Attribution License](https://creativecommons.org/licenses/by/4.0/), which permits use, distribution and reproduction in any medium, provided the original work is properly cited.

Project Administration: T. Bording, A. V. Christiansen, K. Rügge, N. Tuxen, M. Hag
Resources: N. Tuxen, M. Hag
Software: T. Bording, G. Fiandaca
Supervision: P. L. Bjerg
Validation: A. V. Christiansen, K. Rügge, N. Tuxen, M. Hag, P. L. Bjerg
Visualization: L. Lévy
Writing – original draft: L. Lévy
Writing – review & editing: L. Lévy, R. Thalund-Hansen, T. Bording, G. Fiandaca, K. Rügge, N. Tuxen, M. Hag, P. L. Bjerg

aquifer and reagents took place, because it allows to react and plan a reinjection shortly after or change the injection strategy. Sampling-based approaches provide accurate information about chemistry changes occurring at a given location, yet with a limited spatial and temporal resolution (Johnson et al., 2015). Decision-support tools for short-term assessment of reagent delivery are needed (Grieger et al., 2010).

Electrical resistivity tomography (ERT) imaging has the potential to provide a rapid, spatially continuous, and well-resolved assessment of the reagent distribution, using the electrical signature of remedial amendments (LaBrecque et al., 1996; Singha & Gorelick, 2005; Slater et al., 2002). Induced polarization (IP) tomography senses the ability of the subsurface to temporarily store electric charges and thus has the potential to detect electrically chargeable ZVI particles (Joyce et al., 2012; Shi et al., 2015; Slater et al., 2005). An additional benefit is that it can help evaluate hydraulic conductivity (e.g., Binley et al., 2016; Fiandaca et al., 2018b; Weller et al., 2015). Recent studies show encouraging results for monitoring the injection of ZVI reagents with surface time-lapse ERT/IP (Flores Orozco et al., 2015, 2019; Nivorlis et al., 2021). Surface ERT/IP imposes a trade-off between spatial resolution and depth of investigation, due to the attenuation of current injected from the surface. This is particularly problematic when the target volume is below 10-m depth and in an area with dense infrastructure where limited space is available to lay out surface cables. In addition, the concrete cover and presence of buried infrastructure at shallow levels (drainage and drinking water pipes, power cables) in urban areas negatively impact the data quality when electrodes are at the surface (see, e.g., Nivorlis et al., 2019).

Data quality, spatial resolution, and sensitivity for deep targets can improve dramatically when electrodes are installed in boreholes (Daily & Ramirez, 1995). Cross-borehole ERT has been successfully used to monitor the migration of saline tracers in well-controlled tank experiments (Slater et al., 2002) and in the field (Singha & Gorelick, 2005; Wilkinson et al., 2010). It has also been installed at contaminated sites to monitor groundwater changes related to in situ remediation (Bording et al., 2021; Nivorlis et al., 2019). However, a largely missing step in surface and cross-borehole ERT/IP investigations is to integrate these methods as impactful decision-support tools for remediation (Singha et al., 2015). In addition, the high-pressure injection of a slurry of ZVI particles in subsurface systems of intermediate permeability (5×10^{-7} – 5×10^{-5} m/s) presents particular challenges not addressed in previous studies, such as complex water chemistry, geological heterogeneities, and unintentional engineered fractures (Velimirovic et al., 2014). Monitoring such an injection requires a multidisciplinary and rigorous strategy, where cross-borehole ERT/IP has great potential. We present here the outcomes and lessons learnt from a pilot-scale field trial in Denmark, where cross-borehole ERT/IP was part of the monitoring strategy after injection of reagents. We illustrate the impact that cross-borehole ERT/IP images can have in practice on remediation operations, as well as report their limitations in practice. Since adequate delivery of reagents is a universal challenge associated to in situ remediation (Christiansen et al., 2010, 2012; Flores Orozco et al., 2015; Stroo & Ward, 2010), these results are relevant for assessing and improving the performance of all in situ remediation operations, including in situ chemical oxidation, enhanced reductive dechlorination, and various ZVI treatments (microscale or nanoscale iron).

2. Materials and Methods

This study was carried out in an aquifer in Farum, Denmark, and is part of a development project by the Capital Region of Denmark. The overall pilot project aims at testing and developing new in situ remediation methods for chlorinated solvent groundwater contamination, including the development of efficient performance monitoring and assessment technologies in complex urban settings.

2.1. Site Description

2.1.1. Site and Geological Settings

The pilot-scale test site is located on a private and paved parking lot with a complex infrastructure including electricity cables, pipes, and drainage systems. The shallow subsurface is dominated by Quaternary sediments (Figure 1). A 10-m section of the subsurface, entirely below the water table, is investigated here: from 10 to 20 m below ground surface (mbgs), corresponding to 29–19 m above sea level (masl). Three main geological layers were identified by borehole logs and sediment sample analyses: (a) glacial clayey till above the section investigated, (b) sandy till in the upper part of the investigated section, and (c) glacio-fluvial meltwater sand in the lower part (Figure 1). Preliminary geological investigations show that the transition between the sandy till

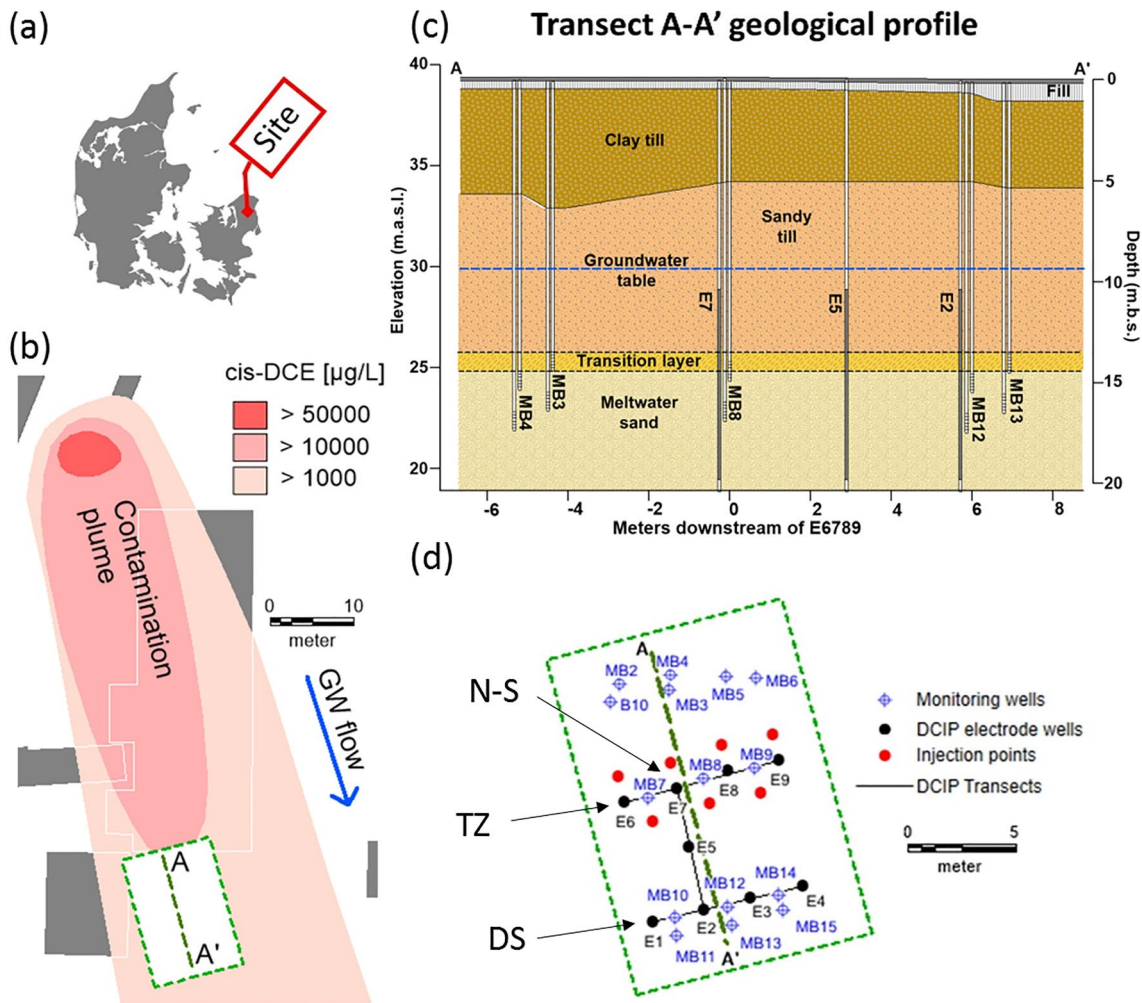


Figure 1. Presentation of the test site. (a) Map of Denmark, with site location highlighted. (b) Zoom on test site showing the contamination plume, buildings (gray boxes), and target area (green rectangle). (c) Geological transect oriented N-S showing three electrode boreholes “EX” and five monitoring wells “MBXX.” Note that the cross-borehole experiment takes place below the groundwater table. (d) Zoom on the target area showing electrode boreholes, injection points, and monitoring wells. Note that injection points are located upstream (north) and downstream (south) of the transect E6–E7–E8–E9.

and meltwater sands occurs between 13 and 14.5 mbs. A thorough classification of the Quaternary sediments in the area can be found in Kessler et al. (2012). Two short-term pump tests were carried out prior to this study both at the source and in the treatment area, showing hydraulic conductivities in the meltwater sand in the range $4\text{--}8 \times 10^{-5}$ m/s (Hovedstaden, 2019).

2.1.2. Contamination

The site hosted a packaging and plastic factory in the period 1959–1989. Several hot spots with groundwater contamination have been identified in the source area, mainly chlorinated solvents and petroleum hydrocarbons. The TZ in this experiment is located in the contaminant plume, 50 m down-gradient of the source. Therefore, no dense nonaqueous phase liquids (DNAPL) is present in the target contaminated groundwater. The contaminant plume mainly consists of chlorinated ethenes in the water phase, reaching a concentration of up to 15,000 μg/L for cis-DCE (dichloroethene) and 6,600 μg/L for TCE (trichloroethylene) before remediation.

2.2. Injection of Reagent

The antimethanogenic chemical reduction agent Provect-IR® (www.provectusenvironmental.com) was injected along with the nonpathogenic bacterial culture KB-1® (www.siremlab.com/kb-1-kb-1-plus/). Provect-IR®

Table 1
General Composition of Provect-IR[®], Given by the Manufacturer and Analyzed in This Study by Inductively Coupled Plasma-Optical Emission Spectroscopy

Compound	%	Source
mZVI	5–90	Manufacturer
Calcium dipropionate	2–12	Manufacturer
Yeast extracts	<2.5	Manufacturer
Guar gum	<2.5	Manufacturer
Sodium sulfite	<2.5	Manufacturer
Fe	45	This study
Total (Ca + K + Mg + Na + S)	2.5	This study
Total carbon	19.5	This study
Unknown	34	This study

Note. Note that elements such as Cl, H, O, P, and N were not analyzed.

consists of a microscale ZVI, calcium dipropionate, yeast extracts, guar gum, and sodium sulfite (Table 1). A combination of abiotic and biotic processes is expected to take place upon injection of Provect-IR[®] and KB-1[®] into the chlorinated ethene contamination. This injection leads in particular to reductive dechlorination, which degrades chlorinated ethenes into “harmless” ethene/ethane through the exchange of chlorine atoms with hydrogen atoms (Stroo & Ward, 2010). Reductive dechlorination requires strongly reducing conditions, electron donors (organic substrates/hydrogen, H₂), and dechlorinating bacteria, which are created by the ZVI donor and KB-1[®] culture injected (Scheutz et al., 2008). The substrates/electron donors can undergo fermentation processes, where bacteria break down organic matter into sugar, amino acids, and lipids that are further fermented into volatile fatty acids (Jørgensen et al., 2005). One fatty acid, propionate, is also added directly in Provect-IR as calcium dipropionate.

Reagent injection took place in August 2019 through seven injection wells, in the depth range 13–17 m (red dots on Figure 1d). The injection pressure was in the range of 3–5 bars, while the flow rate varied from 6–11 to 9–19 L/min. Injection was carried out from the bottom of the well and up while withdrawing. Several daylighting events (transport of ZVI up to the surface) were witnessed during the injection and may have created upstream passages.

2.3. Geo-Electrical Methods for Environmental Applications

In an electrical context, geological formations can be thought of as a combination of resistors and capacitors. Ions in pore water and those connected to clay minerals are charge carriers in aquifers. Conductive water and clay minerals can be represented by conductors with high conductivity, as opposed to freshwater and pure quartz sand or gravel, which have lower conductivity. All interfaces favor the accumulation of ions, e.g., between pore water and sediment matrix, which is similar to the effect of a capacitor in an electronic circuit and is called polarization. The larger the total pore surface area, the more charge accumulation is possible (Weller & Slater, 2019). Semiconducting metallic particles (e.g., pyrite or ZVI) also cause electronic conduction and polarization. Polarization caused by semiconductor is usually several orders of magnitude stronger than sediment/water interfaces, due to the possibility of electron redistribution within their crystal structure (see, e.g., Revil et al., 2017; Slater et al., 2005, 2006). Therefore, the conduction and polarization properties of the subsurface can reflect parameters such as iron content, hydraulic conductivity, and changes in pore water chemistry (Table 2).

In the absence of clay minerals and metallic particles, the electrical charge carriers are predominantly ions in pore water. In this case, the total aquifer electrical conductivity, also called “formation conductivity,” is proportional to the electrical conductivity of pore water and thus to the concentration of major ions (Archie, 1942; Maurya et al., 2018). In sedimentary contexts, the amplitude of polarization created by the application of an electric field in the aquifer can be translated into hydraulic conductivity, provided that several conditions are met (Robinson et al., 2018; Weller & Slater, 2019; Weller et al., 2015). Situations where hydraulic conductivity calculation from DCIP is not possible include very conductive environments (e.g., in highly altered faciès where smectite is dominant or in saltwater-dominated aquifers), where the voltage signal level becomes too low (Lévy et al., 2019b), as well as environments with metallic particles, as they strongly contribute to the polarization signal (Lévy et al., 2019a). Note that hydraulic conductivity estimated from polarization measurements do not account for thin fractures.

ERT consists of injecting a direct current (DC) through two current electrodes (A and B) and measuring the resulting voltage at two potential electrodes (M and N). The time-domain induced polarization (TDIP) method consists of recording the same voltage signal $V(t)$ but with a high sampling rate and focusing on the discharge after current turn-off. Charge and discharge curves are represented by the chargeability, which is equal to $V(t)$ divided by the primary voltage, V_p , after current turn-off (Bertin & Loeb, 1976; Sumner, 1976). The term DCIP indicates that DC and IP are combined in the same measurement cycle. The voltage time series were recorded with the Terrameter LS instrument at a sampling rate of 3,750 Hz, with 2 s on-time and postprocessing was applied to the voltage signal, in particular to remove spikes and 50 Hz harmonics (Olsson et al., 2016).

Table 2

Principle of the DCIP Method: Physical Processes Proposed by the Scientific Community, Parameters Measured, and Corresponding Environmental Parameter With Potential Applications

Physical process	Electric charge carrier	DCIP param.	Environmental param.	Possible environmental applications	References
Electrolytic conduction	Ions in pore water	ρ or σ'	Equivalent ion concentration	Mapping contamination Monitoring distribution of reagent	Archie (1942), Balbarini et al. (2018), and Maurya et al. (2018)
Surface + interfoliar conduction	Ions in clay minerals	ρ or σ'	Cation exchange capacity	Mapping clay caps (volcanic). Mapping lithological contrasts, e.g., clay layers	Lévy et al. (2018) and Waxman and Smits (1968)
Electronic conduction	Electrons in connected metallic minerals	ρ or σ'	Volume of metallic particles	Mapping and monitoring distribution of large metallic clusters (sulphides, solid iron)	Pridmore and Shuey (1976), Shuey (1975), and Slater et al. (2006)
Ionic polarization	Ions adsorbed at solid surface and in pore water	Φ_{\max} or σ''	Pore surface area	Mapping hydraulic conductivity	Bücker and Hördt (2013), Fiandaca et al. (2018b), and Weller et al. (2015)
Electronic polarization	Electrons in disseminated metallic minerals	Φ_{\max} τ, C	Volume of metallic particles Grain size of metallic particles	Mapping/monitoring distribution of disseminated metallic particles	Lévy et al. (2019a), Pelton et al. (1978), and Slater et al. (2005)

Note. The last column gives a nonexhaustive reference list for further information on the processes and the conversion from DCIP to environmental parameters. DCIP parameters are: resistivity ρ , real conductivity σ' , imaginary conductivity σ'' , maximum phase angle Φ_{\max} , relaxation time τ , and Cole-Cole exponent C .

The wide range of geological, mineralogical, and chemical features that affect the electrical signal (Table 2) is both the main strength and the main limitation of the method, due to nonunique interpretation of geophysical signals.

2.4. Cross-Borehole ERT and TDIP

2.4.1. Data Acquisition

Three types of electrode configurations, further illustrated in Supporting Information S1, are used in this study: (a) “single-borehole,” where the four electrodes are in one borehole, (b) “AB-MN,” where the current dipole is in one borehole and the voltage dipole in another one, and (c) “AM-BN,” where current is sent between two boreholes and voltage measured between the two same boreholes (Bing & Greenhalgh, 2001; Bording et al., 2019). Nine boreholes were installed in June 2019, with 32 stainless steel ring electrodes in each. The distance between neighboring boreholes is in the range 2.5–3 m, and the vertical spacing between electrodes is 0.3 m. All electrodes are installed in the depth range 10–20 m. Data were combined into three 2D profiles: (a) E6–E7–E8–E9 (profile running West-East in the TZ, hereafter called TZ transect), (b) E7–E5–E2 (profile running North-South, parallel to the natural hydraulic gradient, hereafter called N-S transect), and (c) E1–E2–E3–E4 (profile parallel to the TZ transect, 7 m to the south, hereafter called the downstream (DS) transect). For each pair of neighboring boreholes, the same quadrupole series was used, including single-borehole, AB-MN and AM-BN configurations. The complete quadrupole series for a pair of boreholes, together with the protocol and spread files for the ABEM Terrameter LS2 instrument are publicly available on the repository attached to this article (see 10.5281/zenodo.7014792). Three borehole pairs were measured for each transect: E6–E7, E7–E8, and E8–E9 for the TZ transect, E1–E2, E2–E3, and E3–E4 for the DS transect and E2–E5, E5–E7, and E2–E7 for the N-S transect. Ten rounds of cross-borehole DCIP acquisitions were carried out, including two before injection of reagent (Table 3). The initial contact resistances of the borehole electrodes were in the range 100–500 Ω before injection and dropped below 100 Ω at levels most affected by injection. Technical issues occurred at R2 and R6 (see Table 3).

2.4.2. Data Processing and Inversion

Apparent resistivity data are shown in Figure S1.2 in Supporting Information S1. The data were first processed manually, where data points with apparent resistivity above 1,000 Ωm and below 1 Ωm are removed. The interval 1–1,000 Ωm was evaluated as a good indicator of decent data quality based on full waveform and pseudo-section

Table 3
Overview of Geophysical Data Acquisition and Chemical Sampling

Round	Date	Days	TZ transect	N-S transect	Downstream transect	Water sampling	Extraction of sediment core
R1	15/07/2019	Baseline	X	X	X	X	—
R2	02/08/2019	Baseline	—	—	—	—	—
R3	08/08/2019	Baseline	X	X	X	—	—
R4	30/08/2019	Inj#1 + 1	X	X	X	—	X
R5	10/09/2019	Inj#1 + 14	X	X	X	X	—
R6	02/12/2019	Inj#1 + 90	X	—	—	X	—
R7	02/06/2020	Inj#1 + 270	X	X	—	X	—
R8	01/12/2020	Inj#1 + 450 (new baseline)	X	X	—	X	—
R9	15/01/2021	Inj#2 + 22	X	X	—	X	—
R10	20/09/2021	Inj#2 + 260	X	X	—	X	—

Note. The double thick line indicates the injection (27–29/08/2019 and 17–19/12/2020). The availability of good quality DCIP data available at the three transects is marked with Xs in columns 4–6.

manual inspection. Hereafter an iterative inversion-based procedure is employed, where data points with the largest contribution to the total misfit are removed. The average data fit is improved after poorly fitted data are removed, and the remaining data are better fitted (Figure S1.4 in Supporting Information S1). The overall quality of TDIP discharge curves was good (Figure S1.3 in Supporting Information S1).

The inversion of resistivity and chargeability data was performed using AarhusInv. The interested reader is referred to Auken et al. (2014) for inversion and Fiandaca et al. (2013) for forward modeling of cross-borehole data and Jacobian computation. The specific borehole implementation (buried electrodes) is presented in Bording et al. (2019). The forward response is calculated in 2.5D along a given profile, assuming that the 2D model extends indefinitely in the direction normal to the profile plane, and electrodes are modeled as points. The boreholes replacing the local geology are composed of PVC tubes, filled with sand of similar composition but not identical to the original formation. Therefore, inversion results include artifacts close to the boreholes (Nimmer et al., 2008). Artifacts on model cells close to the boreholes may also stem from uncertainty on electrode position, which affects more data with small spacing (Wilkinson et al., 2008).

The model mesh for inversion is composed of 0.15×0.5 m cells (thickness \times width), corresponding to 28 model columns in each profile and 78 layers between the uppermost and bottom electrodes. Electrodes need to be on a node in the model and forward meshes. We chose two nodes per electrode spacing in the vertical direction, as one was not accurate enough, and three was computationally too expensive.

The parameters in each model cell are constrained to the neighboring cells in the vertical and horizontal directions. In the model space, the frequency-dependent complex conductivity σ^* is described through a reparameterization of the Cole-Cole model, the maximum phase angle (MPA) model, which is considered to yield better-resolved parameters (Cole & Cole, 1941; Fiandaca et al., 2018a). The MPA model consists of four parameters: the resistivity ρ , the maximum phase angle ϕ_{\max} , the relaxation time τ , and the Cole-Cole exponent C . ϕ_{\max} is particularly adapted for emphasizing disseminated metallic particles (Lévy et al., 2019a).

The so-called “time-lapse” inversion follows Fiandaca et al. (2015), in a cascaded inversion scheme. The starting model of the inversion is the final model of a reference round. The new model is constrained to the baseline model through the asymmetric minimum support norm. This time-lapse inversion scheme focuses the time-lapse changes, retrieving the smallest model differences compatible with the data. On the other hand, with the so-called “standalone” inversion, no constraints to the starting model are imposed.

The standard deviations on resistivity and chargeability data are calculated following Olsson et al. (2016), summing a uniform relative standard deviation $\sigma_{rel,uni}$ to a voltage-dependent relative standard deviation $\sigma_{rel,V}$,

which takes into account the measurement voltage level V , the duration of measuring gate T_{gate} , the stack size n , and the voltage noise level V_{noise} . Equation 1 presents how $\sigma_{rel,V}$ is calculated

$$\sigma_{rel,V} = \frac{V_{noise}}{V} \sqrt{\frac{1}{n \cdot T_{gate}}} \quad (1)$$

For any datum d , the total standard deviation is calculated as

$$\sigma = d \cdot (\sigma_{rel,V} + \sigma_{rel,uni}) \quad (2)$$

In this work, relative uniform errors $\sigma_{rel,uni} = 2\%$ and 10% were used for resistivity and IP data, respectively. A voltage threshold $V_{noise} = 2$ mV was used for all data. Figure S1.4 in Supporting Information S1 illustrates the dependency of the standard deviation on the voltage measured.

The data misfit χ is calculated as

$$\chi = \sqrt{\frac{1}{N} \sum_{i=1}^N \left(\frac{d_i - f_i}{\sigma_i} \right)^2} \quad (3)$$

where N indicates the number of measurements, d_i , f_i , and σ_i represent the i th datum, forward response, and standard deviation, respectively. This equation is used for ERT data (resistivity) and TDIP data (chargeability of any gate) separately, as well as combined.

In the rest of the study, we focus on the conductivity parameter which is the inverse of the resistivity, as it is more relevant for comparison to chemical parameters.

2.5. Chemical Analysis of Groundwater and Sediment Samples

Table 3 summarizes the sampling rounds of water and sediments in monitoring wells. Upstream and downstream monitoring wells were installed before the start of injection, while monitoring wells inside the TZ (MB7, MB8, and MB9) were installed after the injection to avoid daylighting through these wells. Sediment cores were extracted from MB7, MB8, and MB9 and analyzed for magnetic susceptibility and solid iron content. Magnetic susceptibility provides a low-cost continuous 1D image of relative solid iron concentration in the cores, while direct measurement of solid iron concentration gives an absolute value in specific points. Details about solid iron measurements are described by Christensen (2020). All water chemistry analyses are presented in Tables S61–S6.4 in Supporting Information S1. The most relevant for comparison with DCIP are presented here: dissolved iron (Fe(diss)), nonvolatile organic carbon (NVOC), calcium (Ca^{2+}), hydrogen carbonate (HCO_3^-), chloride (Cl^-), ionic strength (I), water electrical conductivity (EC).

2.6. Hydraulic Conductivity

2.6.1. Estimation From Sediment Samples

Sediment cores extracted from the TZ provided a total of 31 samples: 6 samples from MB7, 10 samples from MB8, 11 samples from MB9, and 4 samples from an additional borehole near MB7. Grain size distribution was obtained by sieving analysis for grain diameters from 2 to 0.063 mm and by laser diffractometer from 0.063 mm to 0.02 μm (Switzer & Pile, 2015). Hydraulic conductivity is estimated from these grain size analyses, following the empirical methods developed by Devlin (2015), where a range of empirical formulas are tested for each sample and a validation criterion is evaluated. The geometric mean is then calculated for all equations where the validation criterion is met. An example of equation, developed by Vuković and Soro (1992), which meets the validation criterion for all samples in this study, is presented in Text S7 in Supporting Information S1.

2.6.2. Estimation From Cross-Borehole DCIP

The hydraulic conductivity estimation relies on laboratory-based relationships established for unconsolidated sediments by Weller et al. (2013, 2015) that link electrical properties and permeability

$$K = \frac{Dg}{\mu} \cdot 3.47 \times 10^{-16} \cdot \frac{\sigma_0^{1.11}}{\sigma''^{2.41}} \quad (4)$$

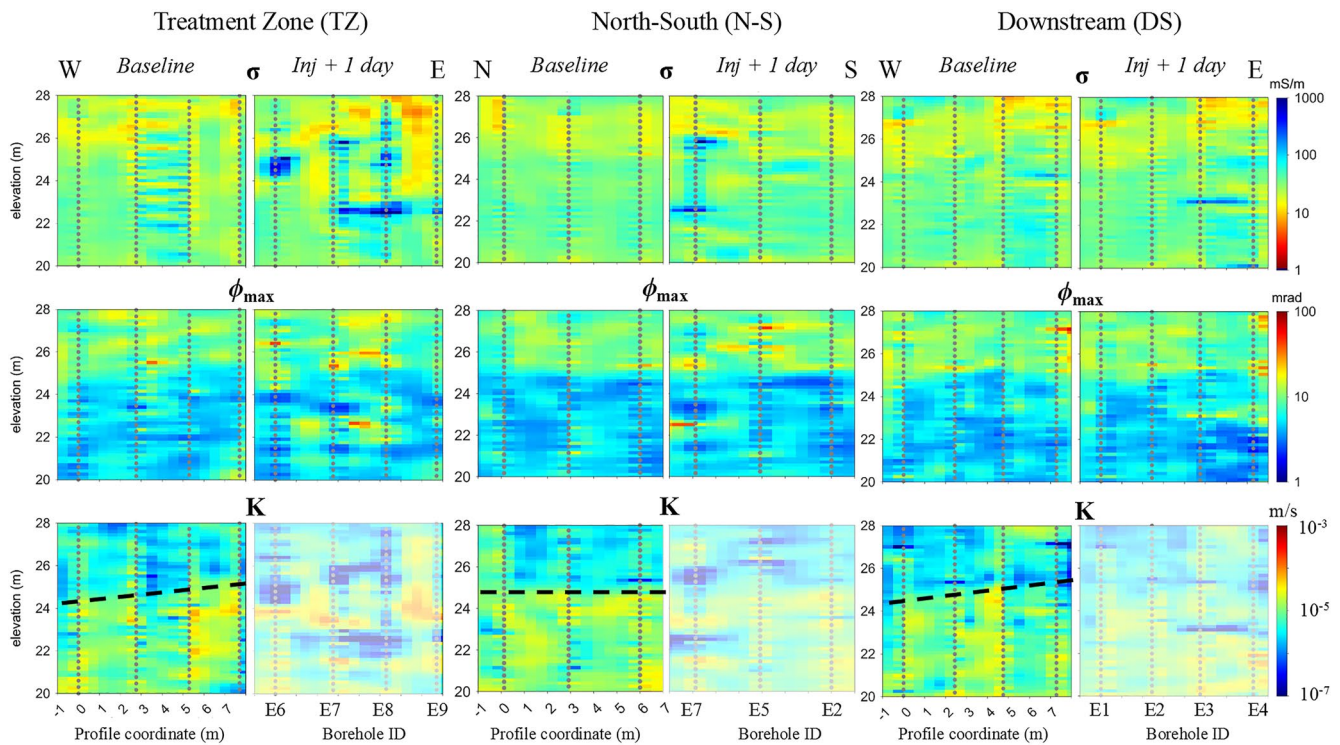


Figure 2. Standalone Direct Current / Induced Polarization (DCIP) inversion results for the three transects at R3 (baseline) R4 (injection + 1 day). The top, middle, and bottom rows show the conductivity σ , maximum phase angle ϕ_{max} , and hydraulic conductivity K obtained with the MPA parametrization. Gray dots show the location of electrodes. The broken black line on the K transects at round three indicate the geological boundary inferred from the inversions—it is only a guide for the eye. At R4, K transects are shaded as we consider that the DCIP conversion to K values is not valid in the postinjection context.

where σ_0 is the real conductivity and σ'' the imaginary conductivity, calculated as $\sigma_0 = \frac{1}{\rho}$ and $\sigma'' = \frac{\phi_{max}}{\rho}$. The permeability is further converted to hydraulic conductivity, using $\frac{Dg}{\mu} = 7.7437 \times 10^4 \text{ cm}^{-1} \text{ s}^{-1}$, where D and μ are the density and viscosity of water at 11 °C, respectively, and g is the gravity acceleration. In practice, the K -distribution only weakly depends on salinity variations. Further details can be found in Bording et al. (2021) and Fiandaca et al. (2018b).

3. Results

The inversion of cross-borehole DCIP data for the three transects at rounds 3 (baseline) and 4 (1 day after first injection) are presented in Figure 2.

3.1. Hydraulic Conductivity Field in the Baseline With Cross-Borehole DCIP

We first analyze the hydraulic conductivity estimations in the baseline, where requirements for hydraulic conductivity calculation from DCIP data are met: sedimentary context with relatively low and spatially uniform ionic conductivity (Table S6.1 in Supporting Information S1), no metallic particles, and little to no clay minerals. Using baseline DCIP data, we observe two distinct ranges of K values (Figure 2): 10^{-7} – 5×10^{-6} m/s in the upper part and 5×10^{-6} – 10^{-4} m/s in the lower part, with a transition at around 25.5 masl. We infer a geological boundary in the baseline based on this contrast. Figure 2 shows that both σ and ϕ_{max} anomalies appear already 1 day after the injection of ZVI, where both ions and metallic particles have been introduced in the aquifer in a nonuniform manner. Therefore, the conditions for K -calculation are not met anymore at R4. This is shown with a shading to illustrate this limit.

To assess the reliability of these DCIP-based hydraulic conductivity estimates “K-DCIP,” we compare K evaluated from grain size analyses (K-GSA) to K-DCIP (Figure 3). K-GSA estimates confirm the trend of lower hydraulic conductivity in the upper part versus higher hydraulic conductivity in the bottom part, with a transition at

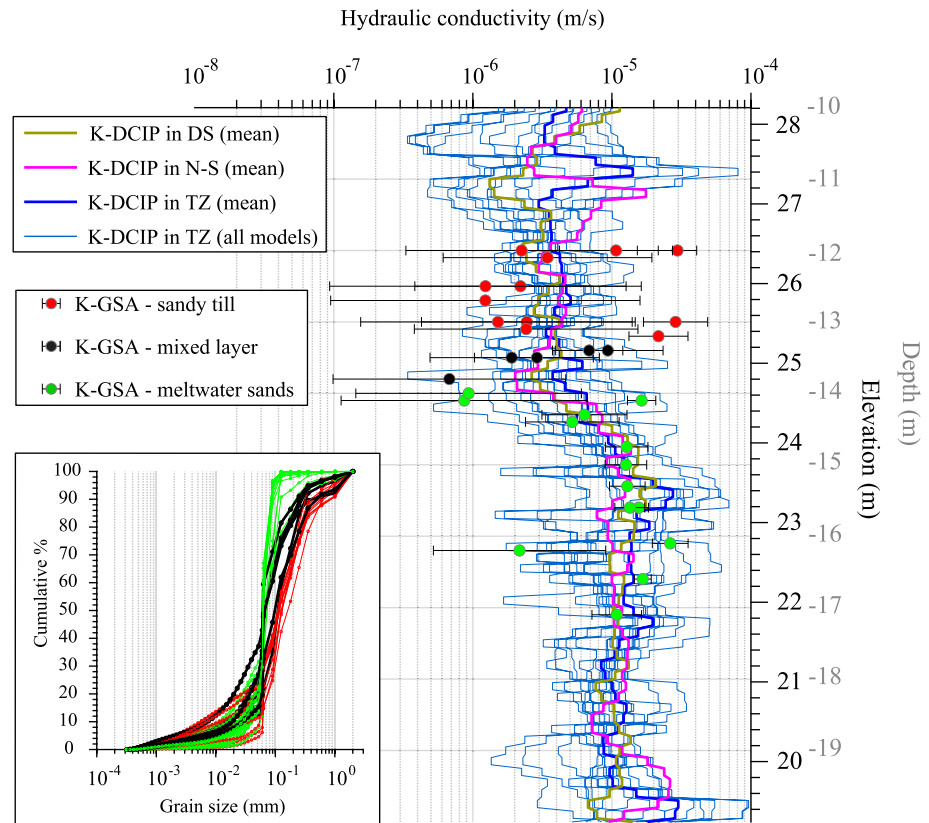


Figure 3. One-dimensional representation of the hydraulic conductivity field, based on estimations from DCIP inversions and grain size analyses (GSA). All vertical models are shown for the TZ transect (thin blue line), and the mean is shown for all three transects (three thicker lines). Both elevation and depth scales are shown, in black and gray, respectively. *K*-estimations based on GSA are represented by filled circles with error bars. The GSA themselves are represented as cumulative percentage, using the same color code, and illustrate a sharp transition at 25.4–25.8 m. The GSA plot includes analyses for 31 sediment samples coming from four boreholes in the TZ.

25–25.5 masl. This transition corresponds to the lithological boundary inferred from DCIP inversions (Figure 2). All boreholes show similar grain size distributions and transition-depth ranges. The bottom layer (meltwater sand) shows a sharp transition at 0.1 mm in the cumulative grain size distribution (Figure 3).

A few outliers are found with higher *K*-GSA values in the upper parts (e.g., at 26–27 masl) and a single sample with lower values in the lower part (e.g., at 23 masl). This type of heterogeneity is expected in a till deposit, where a wide range of grain size distributions coexist, as illustrated by red curves in the GSA cumulative representation (Figure 3). An advantage of *K*-DCIP estimations over point sampling is that it provides a spatial picture of the permeability distribution with a much larger and coherent data set, without significant bias due to local heterogeneity or spatial inconsistencies. The overall agreement between *K*-GSA and *K*-DCIP predictions allows further interpretation of *K*-DCIP distribution in the discussion.

3.2. Influence of Reagent on Water Electrical Conductivity

We show in Figure S4 in Supporting Information S1 the contours of the contaminant plume to allow interested readers evaluating the extent and composition of the contamination. However, we do not expect influence of the contamination neither on the water electrical conductivity (EC) nor on the cross-borehole results, as the chlorinated ethenes are neutral compounds (see further discussion in Section 4.1). Thus, we focus on the electrical response of the reagent.

Once Provect-IR® is injected, the following ions are expected to increase: Ca^{2+} , HCO_3^- , $\text{Fe}^{2+}/\text{Fe}^{3+}$, K^+ , Na^+ , Mg^{2+} , SO_4^{2-} (Table 1). The equivalent conductivity of these ions, calculated with the methodology described by

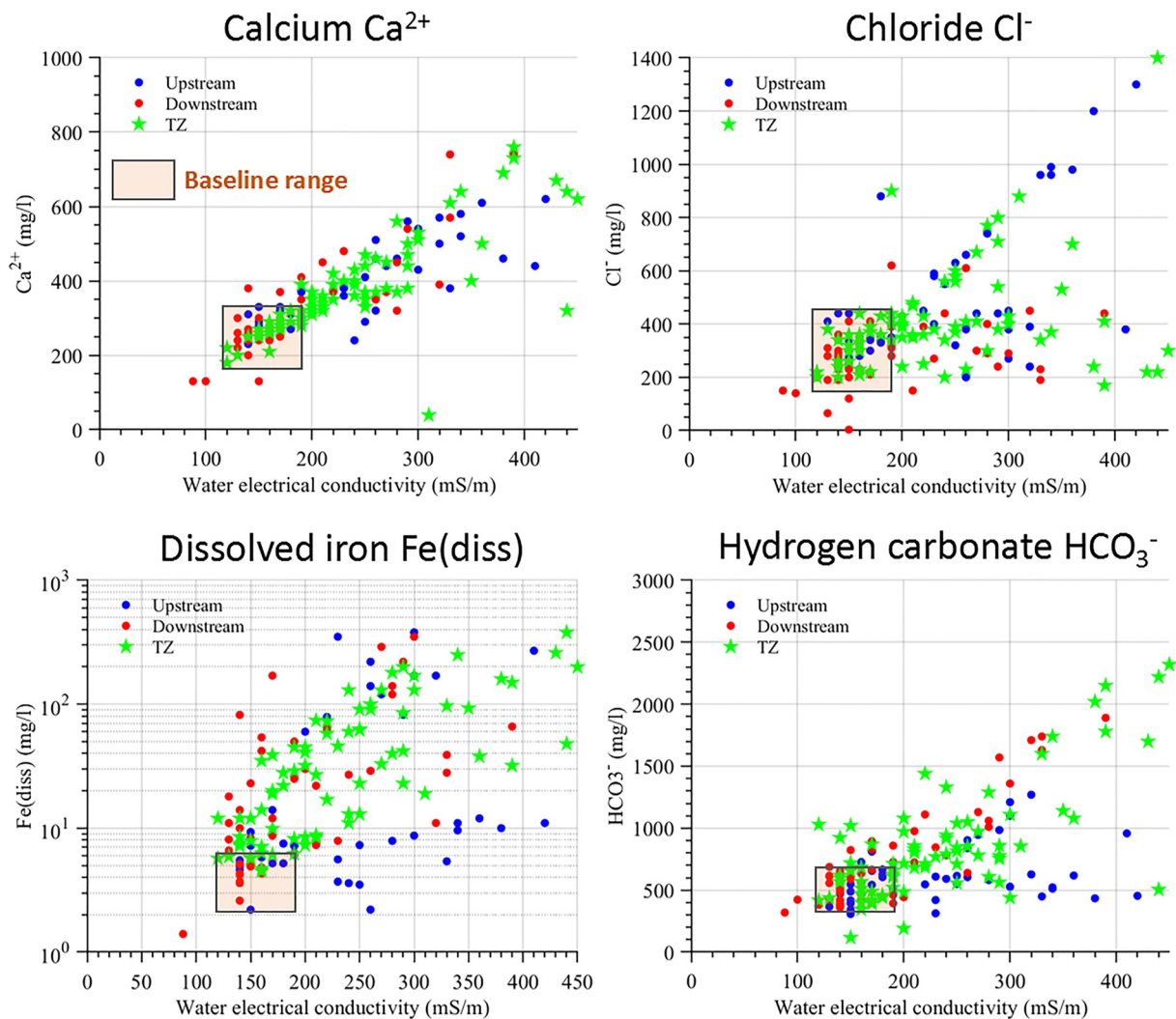


Figure 4. Correlation between electrical conductivity and concentration of four ionic compounds of interest for monitoring the injection and remediation: Ca^{2+} , Cl^- , $\text{Fe}(\text{diss})$, HCO_3^- concentration. Data are measured using groundwater samples from monitoring wells. All available data are plotted together (all wells, all monitoring dates, from R1 to R9, see Table 3). Note that $\text{Fe}(\text{diss})$ concentrations are represented with a logarithmic scale.

Appelo and Postma (2005), is presented in Figure S3.1 in Supporting Information S1, together with that of Cl^- . Figure S3.1 in Supporting Information S1 emphasizes that Cl^- , Ca^{2+} , and HCO_3^- are among the main contributors to water EC. The equivalent conductivity of dissolved iron $\text{Fe}(\text{diss})$ is absent from Figure S3.1 in Supporting Information S1, as it is more complex to calculate.

The concentrations of Ca^{2+} , Cl^- , and HCO_3^- increase by a factor up to 4 after injection, similar to EC increase, while $\text{Fe}(\text{diss})$ is below 10 mg/L in the baseline and increases by up to two decades after injection (Figure 4 and Table S6 in Supporting Information S1). A linear relation is observed between water electrical conductivity and Ca^{2+} in the upstream, downstream and TZ areas for all measuring rounds (Figure 4). Similarly, a clear correlation between EC and HCO_3^- is seen in the TZ and downstream area, but not the upstream area. A clear correlation between EC and Cl^- is observed for a few wells in the TZ and upstream areas, but Cl^- does not increase significantly in the downstream area, while the EC does. The correlation between EC and dissolved iron is clear in the TZ but less clear in the downstream and upstream areas. Finally, a qualitative empirical relation between EC and NVOC is seen (Figure S3.2 in Supporting Information S1), especially in the TZ and downstream areas. Although NVOC is not expected to contribute directly to EC (not ionic), it seems to follow EC variations.

3.3. Monitoring the Remediation Cloud With Cross-Borehole Time-Lapse ERT

The spatial spreading of the reagent is hereafter referred to as the “cloud,” as opposed to “plume” for contamination. Cross-borehole DCIP inversion results, presented in Figure 2 for *R3* and *R4*, show conductivity (σ) changes after injection at several places on the three transects. The clearest changes are in the TZ, as illustrated by blue anomalies on the TZ transect and on the northern part of the N-S transect. A small anomaly is also observed on the DS transect at 23 m elevation. To assess the cloud distribution over time and to subtract the influence of geology on the conductivity contrasts, time-lapse ERT results are presented in Figure 5, using the ratio between postinjection conductivity and baseline conductivity (*R3* is taken as the baseline round). The ratio representation chosen emphasizes in blue high-conductivity anomalies caused by the injection: a darker color corresponds to a larger conductivity increase. The top row in Figure 5 illustrates the natural variability of the ERT signal, using the ratio *R1/R3* (two baseline rounds). The other rows in Figure 5 dynamically show the spreading of the reagent. Some light variations are visible in the TZ transect between *R1* and *R3* and are attributed to data noise. In the rest of our analysis, we focus on anomalies that have a significantly darker color.

Shortly after injection, the conductive cloud imaged by time-lapse ERT anomalies appears at a few high-conductivity anomalies, mainly at 23 and 26 masl (*R5*). Nine months later, it occupies the entire transect length at 23 and 26 masl (*R7*). A progressive filling of the space between boreholes E7 and E8 is also seen during the monitoring period (from *R5* to *R8*). Approximately half of the TZ transect is filled with high-conductivity anomalies at *R8* (15 months after the injection) (*R8*). An overall southwards spreading together with a downwards migration is observed along the N-S transect over the monitoring period. In both the TZ and N-S transect, a white section between 23 and 25 masl still remains at *R8*, indicating no or minimal change in conductivity and thus absence of remediation cloud in this volume. A thin anomaly is seen in the downstream transect at 23 masl between boreholes E3 and E4, already at *R4* (Figure 2) and still at *R5* (Figure 5).

In order to fill the remediation “gap” between 23 and 25 masl, a second injection round was carried out with injection screens focused in this interval (see TZ transect at *R9*). A new baseline was measured (*R8*) and the changes after the second injection show that the reagent follows, again, a preferential pathway above and below the target range (bottom row in Figure 5, ratio *R9/R8*).

3.4. Qualitative Comparison of Remediation Cloud Mapping by Cross-Borehole ERT and by Water Samples

Cross-borehole ERT and water chemistry compare qualitatively well on the TZ, N-S, and DS transects (Figure 6). In particular, limited spreading of the reagent at 23–25 masl is confirmed by chemical monitoring both on the TZ and N-S transects. The increased concentration of Fe(diss) at *R5* in screen MB13-1 matches exactly the conductive anomaly inferred from ERT on the DS transect. However, this chemical increase is not reflected on the N-S transect. Note that screens projected on the N-S transect are up to 2 m away from the transect plane and thus local anomalies might not be captured. In the N-S transect, no geophysical data are available north of E7, but monitoring screens show a clear increase of chemical compounds related to the reagent, especially at 22 masl (Figure 6, see also Table S6.1 in Supporting Information S1).

Overall, the monitoring screens and cross-borehole ERT show consistent remediation cloud locations. Yet, the 2D anomalies observed with ERT provide a more complete image of the remediation cloud distribution than if based solely on monitoring screens. In order to evaluate whether the remediation cloud is only related to ionic species, we compare in the next section the measured water conductivity in wells and the ERT-derived water conductivity.

3.5. Quantitative Comparison of Water Electrical Conductivity Estimated by Cross-Borehole ERT and Measured by Water Samples

We convert total conductivity into water conductivity following Equation 5 (Archie, 1942), assuming that only ions in pore water contribute to the total conductivity.

$$\sigma_{ERT} = \frac{\sigma_w}{F} \quad (5)$$

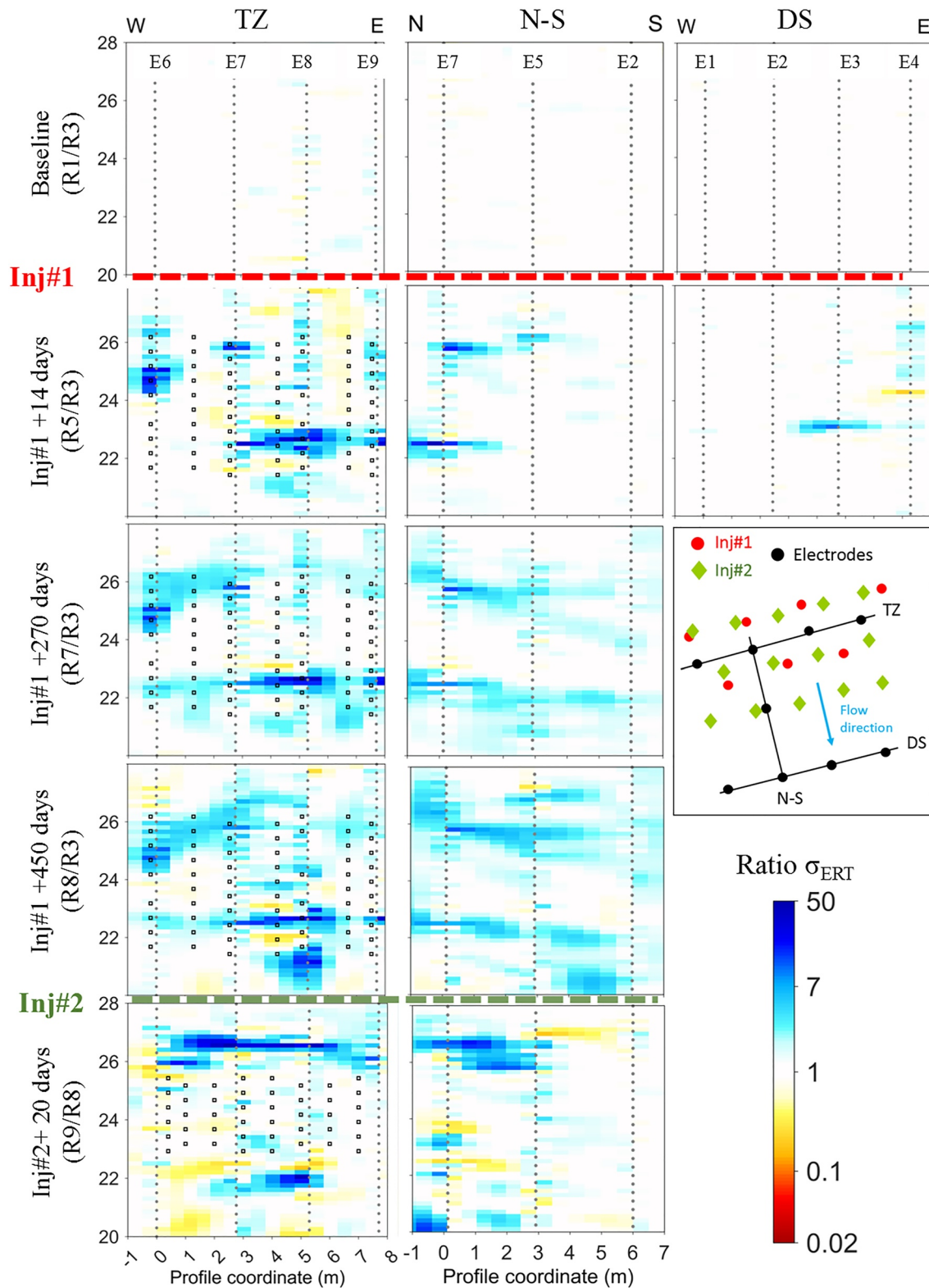


Figure 5. Electrical conductivity ratio for time-lapse ERT (σ_{ERT}) at the three transects, from left to right: treatment zone (TZ), north-south (N-S), downstream (DS). Five rounds are shown: R1, R5, R7, and R8 are compared to R3 (baseline for injection 1 “Inj#1”); R9 is compared to R8 (baseline for Inj#2). The ratio R1/R3 illustrates the natural variability in the baseline. Gray dots indicate electrodes. Injection screens surrounding the TZ transect are projected (black squares); their exact location is shown on the map. The y-scale indicates altitude in meters above sea level (masl).

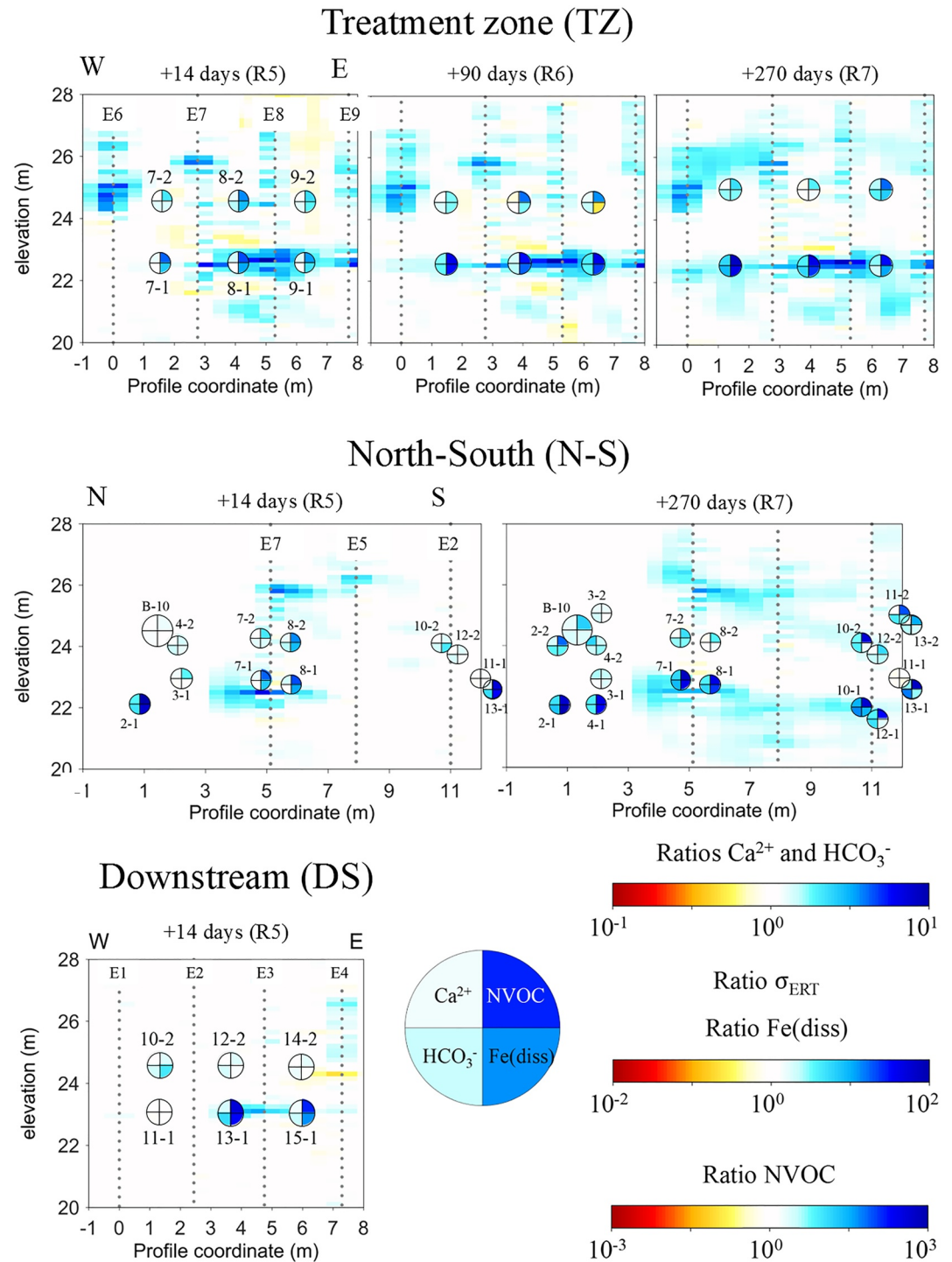


Figure 6. Comparison of electrical conductivity ratios obtained by time-lapse ERT (σ_{ERT}) to concentration ratios of calcium (Ca^{2+}), hydrogen carbonate (HCO_3^-), dissolved iron Fe(diss), and nonvolatile organic carbon (NVOC) obtained by chemical monitoring (see Table S6 in Supporting Information S1 for calculation of baseline values). On the N-S transect, all screens projected are 1–2 m away from the figure plane. This is represented by a slight vertical shift (up for west of the plane and down for east). Most screens cover in reality a 1-m depth range (2 m for B-10). Relevant ID for electrode boreholes and monitoring screens are shown. Three different color scales covering increasing ratio range width: (i) Ca^{2+} and HCO_3^- , (ii) σ_{ERT} and Fe(diss), and (iii) NVOC.

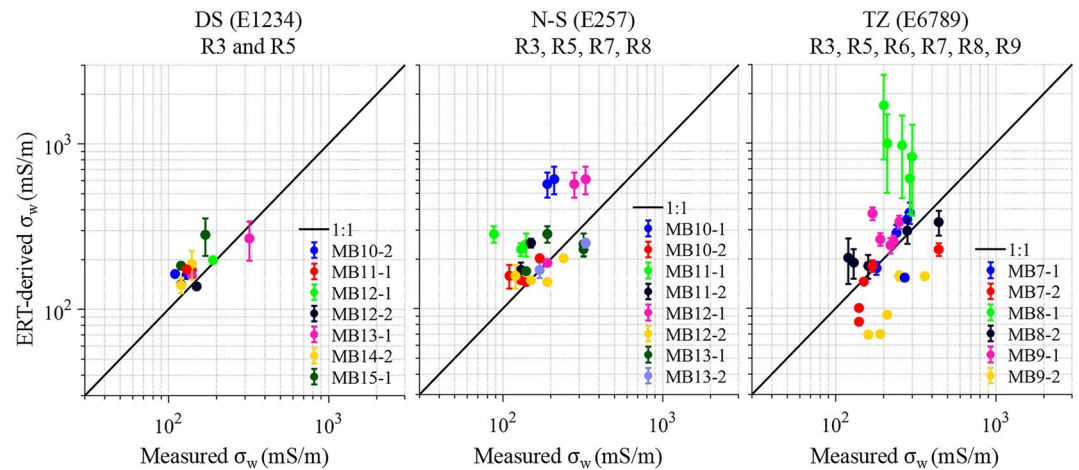


Figure 7. Comparison of σ_w measured in water samples (x axis) and calculated from cross-borehole ERT inversion assuming homogeneous formation factor of 4.5 (y axis). The three transects are shown separately at all rounds where both data are available. The color code corresponds to monitoring screens (see Figures 1 and 7 for positions). Vertical error bars are calculated based on the variance within a set of 14 inverted cells around each screen used for water samples.

where σ_{ERT} , σ_w , and F are the total conductivity inferred from ERT (S/m), the water conductivity (S/m), and the formation factor (dimensionless). We use here a formation factor of $F = 4.5$, which is typical for similar geological sediments in Denmark (Maurya et al., 2018).

At locations where both are available, we compare the measured σ_w in water samples to the ERT-derived σ_w (Figure 7). The absence of clay minerals is a condition of validity for Archie's law. We estimate that this condition is fulfilled in our case, given that (a) the screens where the comparison is carried out are mostly below the sandy till/meltwater sand boundary and (b) ERT-derived and DCIP-derived σ_w show very similar values in the baseline (comparison not shown here). We choose ERT inversions for calculating σ_w , as DCIP inversions are likely affected by a polarization effect from the injected ZVI. An effect of ZVI on ERT inversions is also possible and we discuss this aspect later on.

Only R3 and R5 are shown for the DS transect and allow assessing the consistency between ERT-derived σ_w and measured σ_w in areas that are not or poorly affected by the injection (Figures 5 and 6). A consistent average baseline value at 150 mS/m can be inferred (Figure 7 and Table S6.1 in Supporting Information S1).

For the TZ transect, where effect of the injection is important already at R5, one screen stands out at all rounds: MB8-1. Much higher ERT-derived σ_w are inferred. In addition, large error bars for MB8-1 indicate sharp changes across neighboring cells. This would be consistent with the presence of a local solid iron cluster.

Discrepancy between ERT-derived σ_w and measured σ_w is also observed for the N-S transect at screens MB10-1 and MB12-1, but only at R7 and R8 (Figure 7, N-S transect, blue and pink outliers). This could mean that the remediation cloud has reached the downstream area, as inferred by cross-borehole ERT, but is too far away from the screens to be fully captured by the chemical monitoring.

We investigate further the discrepancy at screens MB8-1, MB10-1, and MB12-1 thanks to magnetic susceptibility measurements and solid iron (ZVI) concentrations in sediments, as well as postinjection IP inversions.

3.6. Comparison to Magnetic Susceptibility and Solid Iron Concentration

Figure 8 reveals that three locations in the TZ contain significantly higher solid iron content compared to the baseline. These anomalies are found in MB7 and MB8 core samples. In MB7, up to 37% of ZVI is observed at 25.6 masl. In MB8, up to 4.7% and 24% are measured at 26 and 22.8 masl, respectively (Christensen, 2020). The baseline is estimated at 0.4–0.9% (higher in the sandy till than in the meltwater sand). These three locations are associated with clear magnetic susceptibility anomalies and correspond to the three main pieces of conductive cloud imaged by σ_{ERT} at R5 and R6 (Figure 8). The high solid iron concentration in MB8 at 22.8 masl is located

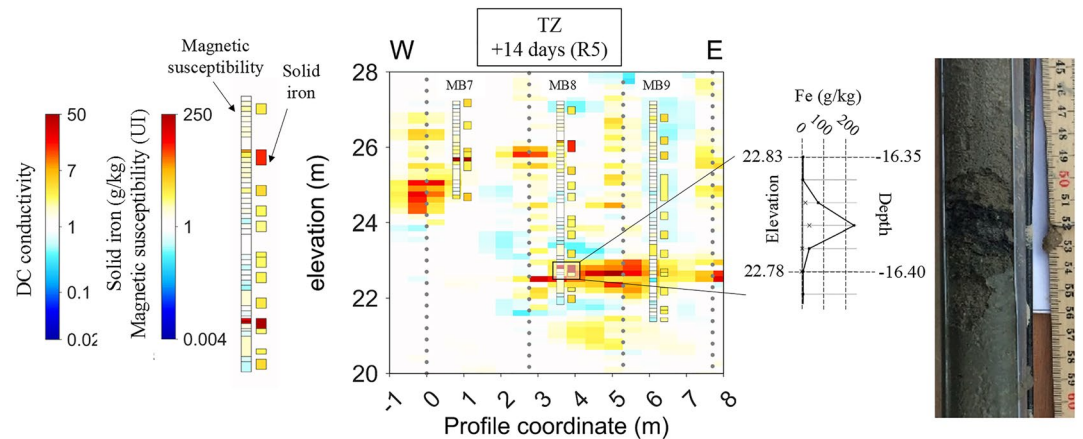


Figure 8. Treatment zone (TZ) after 14 days ($R5$). Core sample analyses in monitoring wells represented on top of the direct current (DC) conductivity ratio $R5/R3$. For each well, solid iron and magnetic susceptibility measurements are shown with the same color scale. The position of the outlier monitoring screen on Figure 7 is highlighted with a black box (screen MB8-1, see also Figure 6). A zoom on the solid iron measurements at this specific location is presented together with a picture of the corresponding core sample.

where the largest discrepancy between measured σ_w (MB8-1) and ERT-derived σ_w is seen (Figure 7). We present a hypothesis to explain these observations in the discussion.

3.7. Changes in IP After Injection

The presence of a solid iron related anomaly can be further assessed by IP results. First, an increased ϕ_{max} is observed in the TZ and N-S transects after injection at elevation 23 m, near borehole E7 (Figure 2). This feature is also associated to an increased relaxation time τ and decreased Cole-Cole exponent C in the same area (Figure S8.1 in Supporting Information S1), which indicates an increased polarization effect. Moreover, this change seen in inversion results is confirmed by increased chargeability data from $R3$ to $R4$, at electrodes located close to the high ϕ_{max} in the inversion model (Figure S9.1 in Supporting Information S1). The location of this IP anomaly matches the cluster of solid iron (Figure 8) and monitoring screens where Archie's law overestimates σ_w (Figure 7). At later rounds ($R5$, $R6$, and $R7$), no clear ϕ_{max} anomaly is observed (Figure S8.1 in Supporting Information S1). These observations are used to further interpret the cloud composition and migration pattern in the discussion. However, given the relatively large natural variability of ϕ_{max} in the baseline rounds (Figure S5.1 in Supporting Information S1), the interpretation of small IP anomalies is kept to a conservative level.

4. Discussion

4.1. Composition of the Conductive Cloud

It is clear that cross-borehole ERT can provide spatially extensive, information on the reagent delivery. Here, we investigate what can be inferred about the remediation cloud composition, based on cross-borehole DCIP monitoring and chemical analyses.

We note a strong spatial consistency between σ_{ERT} and dissolved iron concentration in all transects (Figure 6), which matches the correlation observed in Figure 4 between dissolved iron and water EC, especially in the TZ and DS screens. Dissolved iron is released by ZVI, both shortly after injection and as a result of slow dissolution. One screen, MB13-1 shows a large increase of dissolved iron without a significant increase of σ_{ERT} in the N-S transect. As mentioned previously, this screen is located 2 m away from the N-S transect. When this screen is compared to σ_{ERT} in the DS transect, the spatial correlation is confirmed.

According to Figure S3.1 in Supporting Information S1, Ca^{2+} and HCO_3^- also have an important contribution to water EC. The spatial correlation between DC conductivity and these ions is very clear in the TZ at $R7$ (Figure 6) although it is less striking than for dissolved iron. It must be noted that the concentrations of Ca^{2+} and HCO_3^- are already relatively high in the baseline, due to the limestone-rich geological formations in the region. The

postinjection increase by a factor up to 4 is related to the reagent itself and to chemical reactions in the aquifer. Ca^{2+} is injected as a counterion for dipropionate, while HCO_3^- is a side product of organic matter fermentation and an electron acceptor in processes following the injection of the reagent (Christensen et al., 2000; Nazaroff & Alvarez-Cohen, 2001). According to Figure 4, water EC changes are following the Ca^{2+} concentration in all screens.

Possible sources of high Cl^- concentration in the background (99–440 mg/L) include road salt for deicing purposes applied during wintertime in the parking lot, as well as dechlorination of chlorinated ethenes (DCE and TCE) to vinyl chloride and ethene. Based on maximum observed DCE and TCE concentrations in the treatment area (15 and 6.7 mg/L, respectively), the maximum chloride increase associated to a complete degradation would be 17 mg/L. In the hot spot itself (upstream), DCE and TCE concentrations reach 86 and 36 mg/L, respectively. A complete degradation would still lead to Cl^- concentration about 20 times lower than observed. Increase of Cl^- concentration after reagent injection (up to 1,700 mg/L in a single screen) could potentially be due to chloride in the reagent itself, but this was not reported by the manufacturer. Thus, the most likely reason for the highly variable chloride concentration is road salt. Only a few screens show a correlation between water EC and Cl^- concentration over time (Figure 4) and no clear spatial correlation with σ_{ERT} is observed (not shown in Figure 6).

Next, we discuss the possible contribution of nonionic species to the σ_{ERT} signal: NVOC increase, degradation of contaminant, and solid iron increase.

We note in Figure 6 an interesting spatial correlation between σ_{ERT} and NVOC: the screens where the most significant NVOC increase is observed are associated to the conductive cloud on all transects (Figure 6). Therefore, the conductive cloud also provides some information about NVOC distribution. However, NVOC seems to have reached areas where no significant σ_{ERT} increases are observed, especially in the upper screens of the TZ transects.

According to several studies, presence of DNAPL might affect the electrical conductivity. For example, simulations by Almpanis et al. (2021) predict that 100% mass removal of a source zone containing 1–60% of DNAPL will lead to a conductivity increase by a factor 2 after 6 years. However, DNAPL is a source zone phenomenon: in contaminant plumes, where the contaminant concentrations are below the free-phase solubility limit, no DNAPL are expected. In our experimental study, where the contaminant plume is treated, contaminants are in the water phase. Both contaminants (chlorinated ethenes) and degradation products (vinyl chloride/ethene/ethane) are uncharged. Chloride release upon degradation, as explained above, has a minor effect on chloride concentration. Therefore, we consider that the contaminant degradation has only negligible effect on the electrical signal. On the other hand, the fermentation of electron donor and organic matter has a significant effect on the electrical signal as charged species, such as hydrogen carbonate and volatile fatty acids, are produced.

Finally, we discuss the influence of solid iron. The main outlier observed on Figure 7 corresponds to screen MB8-1. At this screen all ERT-derived σ_w values after injection are 5–10 times higher than the measured σ_w (Figure 7, TZ transect). At this location, high magnetic susceptibility and concentration of solid iron (24%) are also measured at R5 (Figure 8), indicating a strong effect of the reagent without a clear increase of Ca^{2+} , HCO_3^- (Figure 6) or σ_w (Figure 7). We interpret this deviation as a contribution of connected ZVI particles to σ_{ERT} . Indeed, ZVI particles concentrated beyond a certain percolation threshold, estimated at 30%, may allow an additional conduction path through electrons diffusion (Shi et al., 2015; Slater et al., 2005; Thommerel et al., 2002). This type of deviation was already observed in natural volcanic samples containing connected pyrite veins (Lévy et al., 2018). A total of 4.2 tons of Provect-IR[®] containing 45% of ZVI (Table 1), corresponding to 1,890 kg of solid iron, was injected during the first injection round. Therefore, we find this explanation plausible. Two additional areas with high magnetic susceptibility and solid iron (MB-7, 37%, and MB-8, 4.7%, see Figure 8 at 26 masl) are associated with the largest σ_{ERT} increase (Figures 5 and 6, TZ transect).

The two other screens, MB10-1 and MB12-2, showing slight deviations compared to the N-S transect at R7 and R8 might also indicate that ZVI particles reached these locations after R5. No core samples are available to support this hypothesis. Another possible explanation here could be the distance between the screens and the transect (1–2 m) and the presence of local anomalies.

Originally, the dissemination of ZVI upon injection was expected to cause a strong increase in polarization, especially of the ϕ_{max} parameter. A clear increase of ϕ_{max} is seen in the TZ and N-S transects at 23 masl 1 day

postinjection (Figure 2 and Figure S9.1 in Supporting Information S1), which is consistent with the presence of disseminated ZVI (Flores Orozco et al., 2015). This ϕ_{max} anomaly disappears at later rounds (Figure S8.1 in Supporting Information S1), meaning that no clear polarization signal can be related to the presence of ZVI at R5 (14 days postinjection). We suggest a coexistence of disseminated ZVI and connected ZVI at R4. The disseminated ZVI is then rapidly dissolved and only connected ZVI remains, with sufficient concentration for allowing electronic conduction (30% according to Slater et al. (2005)). This is consistent with the increase of dissolved iron measured in water between R5 and R6 (no chemical data at R4). Another explanation for the absence of clear polarization signals at postinjection rounds is that strong increases of water EC tend to decrease the polarization response of materials, both due to lower voltage injected and higher conductivity of the medium (see e.g., Lévy et al., 2019a, 2019b).

At R5 and later rounds, the areas with 37% and 24% of solid iron (MB7 at 25.6 masl and MB8 at 22.8 masl, respectively) coincide with large σ_{ERT} and relaxation time increases, while there is no clear ϕ_{max} signal (Figures 8 and 6 and Figure S8.1 in Supporting Information S1). In the case of connected particle, a phase-angle increase is generally still expected but it might be relatively small. It was, e.g., observed in frequency-domain data sets that the maximum phase angle can be lower while the pyrite content is higher when pyrite particles are very connected (see Figures 2, 4, and 6 in Lévy et al. (2019a)). An increase of relaxation time for connected ZVI particles was also observed by Slater et al. (2005). This confirms the possible influence of ZVI on the σ_{ERT} and on the relaxation time, rather than on ϕ_{max} . In the future, simpler parametrization of the time-domain decay curves would be interesting, such as those suggested by Martin et al. (2021).

Overall, a quantitative conversion of σ_{ERT} into σ_w is not possible because Archie's law is not strictly verified at all screens, most likely due to the influence of ZVI (solid) on σ_{ERT} .

These observations illustrate that ERT alone cannot capture the complexity of the different on-going chemical processes related to changes in water chemistry. In particular, degradation products and reagent markers cannot be distinguished. Detailed chemical monitoring is needed to discriminate the different ions and understand what processes are at play in the different areas. Nevertheless, we can also conclude that, in the case of ZVI remediation, the conductive cloud mapped with cross-borehole ERT corresponds to an increase of dissolved ions in water (mostly Fe(diss) and to a lesser extent Ca^{2+} and HCO_3^-), as well as an increase of connected ZVI particles whenever Archie's law overestimates the ERT-derived σ_w . The use of magnetic susceptibility measurements allows building confidence in the ZVI particles interpretation. On the other hand, σ_w gives a clear overview of the ionic cloud spreading—all processes combined.

4.2. To What Extent Is the K-DCIP Field Useful in a Remediation Context?

Based on Figure 5, we concluded that the reagent did not spread as expected in the TZ, with in particular a 2 m-thick “blank” section, where no conductivity changes are observed. Similar blank sections are observed in the TZ and N-S transect. This conclusion is supported by chemical monitoring, which shows that screens located in the “blank” section have a very similar chemical composition compared to before injection (Figure 6). After the second round of injection, we see again that the reagent does not spread in this section, although the injection screens were specifically designed to fill the gap (Figure 5, bottom row, showing ratio R9/R8). We investigate whether this behavior could have been predicted before-hand with the *K*-field, by comparing (a) the K-DCIP distribution before injection to (b) the conductivity changes imaged by ERT after injection.

Figure 9 shows the contours of the remediation cloud in R5 and R7 (+14 and +270 days after injection, respectively) on top of the hydraulic conductivity field (R3, before injection). Within the black contours, the formation conductivity has changed by >30% compared to the baseline (R3). We choose this threshold to dismiss anomalies in the range of natural variability (Figure 5, top row showing the baseline ratio R1/R3).

If there was a strict correlation between conductivity changes and *K*-distribution, we should observe maximum spreading in the high-*K* zone (e.g., in the TZ transect, between E8 and E9, 23–24 masl) and limited spreading in the low-*K* zone (upper sandy till where spreading still occurs).

At +270 days (R7), we do see that the conductive cloud flows around (a) a low-*K* block, between E7 and E8, at 25–26 masl on the TZ transect and (b) a horizontal low-*K* lens between E5 and E2 at 25 masl on the N-S transect (Figure 9). However, we see that a major part of the reagent spreads into the less hydraulically conductive sandy

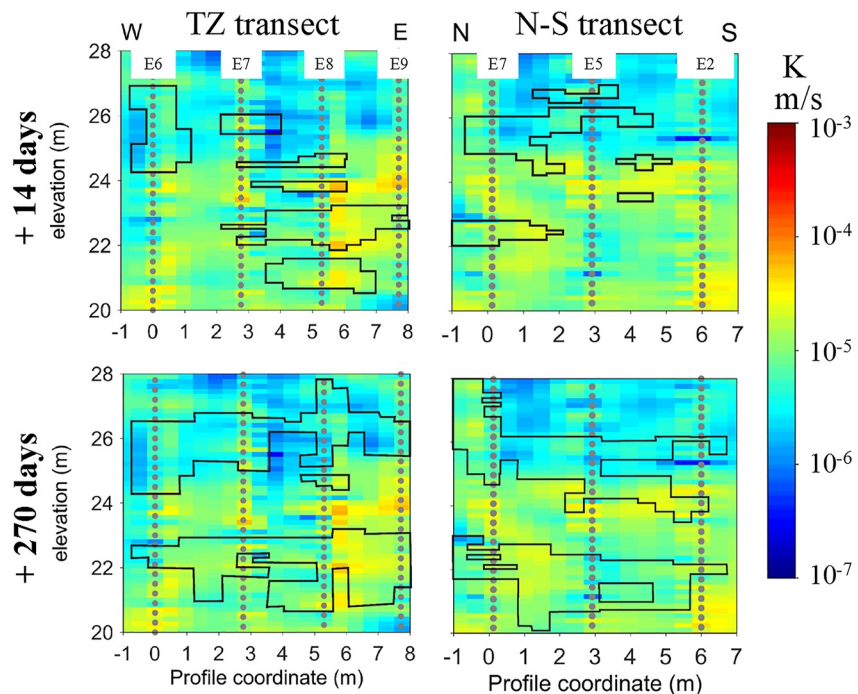


Figure 9. Overlap of the hydraulic conductivity field (background image) by the remediation cloud (area within black contour) at +14 days and +270 days. Left and right panels show the TZ and N-S transects, respectively.

till and the transition layer at 25 masl while it does not clearly spread more in the most permeable areas of the meltwater sand formation.

The observed mismatch can have several explanations. First, small-scale variability in K within a given geological facies, such as illustrated by the GSA (Figure 3), goes beyond the scale of the K-DCIP field. The DCIP method is not sensitive enough to these small-scale heterogeneities, while they might have a strong influence on transport properties and spreading of reagent. Second, IP data are only able to retrieve part of the information needed to understand transport properties, namely the grain size and pore throat diameter distribution (Weller et al., 2015). To the authors' knowledge, no IP study has been able to map fractures or their influence on the hydraulic conductivity field. One can wonder about environments where the initial presence of fractures is less likely to influence the transport and pathways, such as unconsolidated sediments. In such environments, high-pressure injection of viscous material can still unintentionally trigger the opening of preferential pathways, which will then play a large role in flow and transport.

Unintentional fracture creation during injection of ZVI was observed in several remediation studies, including in sandy aquifers (see, e.g., Flores Orozco et al., 2015). This hypothesis is supported by several observations at the study site. First, an upstream leakage of reagent is clearly seen in monitoring screen MB2 for all chemical parameters (Figures 4 and 6). This leakage is consistent with upstream surface spills observed during injection in some of the screens and forcing the on-site team to stop injection in the corresponding depth interval. This depth interval, where overpressure prevented the completion of injection, corresponds to the “blank” sections observed on the TZ transect (Figure 5). Upstream leakage associated to high-pressure injection is a strong indication of pressure-induced fracture enhancement or creation. No electrode boreholes are available upstream to confirm this hypothesis with ERT measurements, since this assumed “leakage” was unexpected. However, the progressive filling of the TZ transect with the conductive cloud, from R5 to R8 (Figure 5) suggests horizontal transport from upstream into the TZ and confirms the upstream rapid leakage. Second, the thin anomaly observed in the downstream transect at +1 day (Figure 2), as well as at +14 days around E3 at 23 masl (Figures 5 and 6) suggests a fast downstream migration. This cannot be attributed to the natural hydraulic gradient, considering the geology and inferred permeability values. Interestingly, the largest ERT anomaly in the TZ transect

is also at 23 masl (Figures 5 and 6). A preferential pathway along this horizon could explain this downstream anomaly.

DCIP predictions of the K -field after injection is delicate since there is a clear influence of the reagent on the conductivity and to some extent the IP parameters. Such calculated K values include a strong bias (shaded panels in Figure 5) and cannot be used. Therefore, it is clear that the K -DCIP field is unable to predict injection paths and explain the reagent distribution in remediation projects involving high-pressure injection. Are then such K -fields estimations useful at all in remediation projects? Future studies addressing geostatistical calculations of flow velocities and contaminant mass discharge estimates, implementing K -DCIP fields, would be useful to allow answering this question further.

4.3. Performance of Cross-Borehole ERT Monitoring Compared to Other Methods

Our study follows the steps of a 20-year old research endeavor on the use of cross-borehole electrical tomography for constraining subsurface hydrological models (Binley et al., 2002; Robinson et al., 2013), as well as monitoring the spreading of saline tracers or CO_2 in targeted aquifers (Carrigan et al., 2013; Perri et al., 2012; Slater et al., 2000).

This study brings novel insights into the performance of cross-borehole ERT for monitoring groundwater remediation, especially in contexts where high-pressure injection is required. Cross-borehole ERT clearly provides a real-time 2D continuous visualization of the remediation cloud spreading, with a high spatial resolution. It outperforms vertical profiling with direct push techniques (e.g., hydraulic profiling, discrete water, and sediment samples), in terms of spatial and temporal resolution and coverage. The 2D images show that reagent spreading is far more complex and heterogeneous than one would assume if the available monitoring screens were interpolated (Figure 6). In the short term, it supports decisions with regards to additional injection and monitoring screens. In the long-term, it can provide information on the migration speed, density sinking, as well as the fate of upstream leakage.

Compared to surface ERT, cross-borehole ERT offers significantly more flexibility and better spatial resolution in the depth range of interest. It is particularly suitable for urban areas where limited space is available for laying out surface electrodes.

Cross-borehole ERT allows assessing the spreading of both the ionic cloud and clusters of solid iron. This cannot be achieved by, e.g., magnetic susceptibility alone, which would only be sensitive to the solid iron. Similarly, chemical analyses of water samples alone do not provide information about clusters of solid iron or spatial distribution of values.

However, in contexts where reagent injection triggers several important chemical changes in the aquifer, cross-borehole ERT does not allow discriminating between species in the ionic remediation cloud. In the case of Provect-IR[®] injection, the ionic cloud is composed of Ca^{2+} , HCO_3^- , $\text{Fe}(\text{diss})$, and to some extent Cl^- and NVOC (Figures 4 and 6, Figures S3.1 and S3.2 in Supporting Information S1). All these species are represented in the conductive cloud imaged by cross-borehole ERT. Furthermore, cross-borehole ERT alone does not allow discriminating between the ionic cloud and clusters of solid iron. Discrete water and sediment samples are needed for that. Future investigations of the IP response of ZVI particles in the field might reveal additional potential of the method to distinguish the ionic cloud from ZVI particles.

In high-pressure injection contexts, given the likelihood of daylighting, cross-borehole ERT monitoring upstream and above the injection would have an additional value to rapidly assess unexpected and problematic flow paths.

5. Conclusion

Conductivity variations measured by cross-borehole ERT provide a visualization tool for the spatial and temporal distribution of ZVI reagent spreading in contaminated aquifers. The injection of Provect-IR[®] reagent, containing 45% of mZVI, leads to the release of ionic species, including Ca^{2+} , HCO_3^- , and $\text{Fe}^{2+}/\text{Fe}^{3+}$, which causes a significant increase of σ_w at places where the product migrates. The ERT-inferred distribution is consistent with chemical monitoring, while providing a more complete image of the remediation cloud spatial distribution.

On the other hand, chemical monitoring allows a sharper understanding of on-going chemical reactions, which cannot be attained by cross-borehole ERT.

Quantitative comparison between measured σ_w in sampling wells and predictions from cross-borehole ERT suggests that other elements than dissolved ions may contribute to the electrical conductivity increase after injection. We hypothesize a contribution from aggregated solid iron particles through electronic conduction. Sediment samples analyses at the study site and laboratory analyses from the literature validate this suggestion.

ZVI remediation leads to unexpected injection paths: daylighting, upstream leakage, and reagent spreading in the TZ through preferred pathways. In order to help achieve a more complete installation of the TZ, the benefit of hydraulic conductivity mapping by DCIP was investigated. The K-DCIP field compares well with K-GSA estimations in the target area, while providing an overview of the K -distribution with a much larger and coherent data set. K-DCIP estimations are less sensitive to local heterogeneity or spatial inconsistencies, which are unavoidable in point sampling. However, the K -field obtained fails at predicting injection pathways and does not help understand the heterogeneous reagent migration. In remediation contexts involving the injection of metallic particles, the K-DCIP field can only be inferred before injection. Therefore, engineered pathways related to high-pressure injection of solid iron are not reflected in the K-DCIP field. In addition, due to the nature of the polarization phenomenon and the limits of electrical tomography in terms of spatial accuracy, the K-DCIP field disregards mm-scale variations in K . Both engineered pathways and mm-scale heterogeneities play a large role in reactive flow and transport, in particular at high injection pressure. Overall, time-lapse conductivity monitoring is most useful to map the injection paths.

Data Availability Statement

More information about DCIP data and inversion can be found in Text S1, S2, S5, S8, and S9 in Supporting Information S1. Details on water chemistry measurements as well as data can be found in Text S3, S4, and S6 in Supporting Information S1. Details on hydraulic conductivity estimations can be found in Text S7 in Supporting Information S1. DCIP data and inversion results, as well as protocol and spread files for the ABEM Terrameter LS2, are available on the repository Zenodo with the following identifier: <https://doi.org/10.5281/zenodo.7014792>.

Acknowledgments

We thank Niklas Marcel Christensen, Jie Zhang, and Vidhi Rathore, M.Sc. students at DTU Environment, for laboratory analysis of Provect-IR[®] content and collection of sediment core samples from the TZ area, as well as Sinh Hy Nguyen, laboratory technician at DTU Environment, for assisting with laboratory analysis of Provect-IR[®] contents and grain size distributions. We also thank Lærke Brabæk Ildvedsen, Morten Dreyer, and Torben Højbjerg Jørgensen at COWI for their contributions to field work and discussion on the data. We thank Pradip Maurya and Anders Kühl, at Aarhus University, for many fruitful discussions and help with IP data processing, as well as Karen Engell Dalsgaard for final proofreading. We finally thank Dimitrios Ntalogiannis, two other anonymous reviewers as well as Associate Editor Sander Huisman for the tremendous reviewing and editing work that has helped greatly improve the quality of the manuscript. This project received funding from the Capital Region of Denmark and Lawyer Thorbergs Foundation.

References

- Almpanis, A., Gerhard, J., & Power, C. (2021). Mapping and monitoring of DNAPL source zones with combined direct current resistivity and induced polarization: A field-scale numerical investigation. *Water Resources Research*, 57, e2021WR031366. <https://doi.org/10.1029/2021WR031366>
- Appelo, C. A. J., & Postma, D. (2005). *Geochemistry, groundwater and pollution* (2nd ed.). Balkema.
- Archie, G. E. (1942). The electrical resistivity log as an aid in determining some reservoir characteristics. *Transactions of the AIME*, 146(1), 54–62. <https://doi.org/10.2118/942054-g>
- Auken, E., Christiansen, A. V., Kirkegaard, C., Fiandaca, G., Schamper, C., Behroozmand, A. A., et al. (2014). An overview of a highly versatile forward and stable inverse algorithm for airborne, ground-based and borehole electromagnetic and electric data. *Exploration Geophysics*, 46(3), 223–235. <https://doi.org/10.1071/EG13097>
- Balbarini, N., Maurya, P. K., Rønde, V., Fiandaca, G., Møller, I., Klint, K. E. S., et al. (2018). Geophysics based contaminant mass discharge quantification downgradient of a landfill and a former pharmaceutical factory. *Water Resources Research*, 8, 436–5456. <https://doi.org/10.1029/2017WR021855>
- Bertin, J., & Loeb, J. (1976). *Experimental and theoretical aspects of induced polarization* (Vol. 1). Schweizerbart Science Publishers.
- Bing, Z., & Greenhalgh, S. (2001). Cross-hole resistivity tomography using different electrode configurations. *Geophysical Prospecting*, 48(5), 887–912. <https://doi.org/10.1046/j.1365-2478.2000.00220.x>
- Binley, A., Cassiani, G., Middleton, R., & Winship, P. (2002). Vadose zone flow model parameterisation using cross-borehole radar and resistivity imaging. *Journal of Hydrology*, 267(3), 147–159. [https://doi.org/10.1016/s0022-1694\(02\)00146-4](https://doi.org/10.1016/s0022-1694(02)00146-4)
- Binley, A., Keery, J., Slater, L., Barrash, W., & Cardiff, M. (2016). The hydrogeologic information in cross-borehole complex conductivity data from an unconsolidated conglomeratic sedimentary aquifer. *Geophysics*, 81(6), E409–E421. <https://doi.org/10.1190/geo2015-0608.1>
- Bording, T., Fiandaca, G., Maurya, P. K., Auken, E., Christiansen, A. V., Tuxen, N., et al. (2019). Cross-borehole tomography with full-decay spectral time-domain induced polarization for mapping of potential contaminant flow-paths. *Journal of Contaminant Hydrology*, 226, 103523. <https://doi.org/10.1016/j.jconhyd.2019.103523>
- Bording, T., Kühl, A. K., Fiandaca, G., Christensen, J. F., Christiansen, A. V., & Auken, E. (2021). Cross-borehole geoelectrical time-lapse monitoring of in situ chemical oxidation and permeability estimation through induced polarization. *Near Surface Geophysics*, 19(1), 43–58. <https://doi.org/10.1002/nsg.12131>
- Bücker, M., & Hördt, A. (2013). Analytical modelling of membrane polarization with explicit parametrization of pore radii and the electrical double layer. *Geophysical Journal International*, 194(2), 804–813.

- Carrigan, C. R., Yang, X., LaBrecque, D. J., Larsen, D., Freeman, D., Ramirez, A. L., et al. (2013). Electrical resistance tomographic monitoring of CO₂ movement in deep geologic reservoirs. *International Journal of Greenhouse Gas Control*, 18, 401–408. <https://doi.org/10.1016/j.ijggc.2013.04.016>
- Christensen, N. M. (2020). *Assessment of field injection and processes in a pilot scale remediation with microscale zero valent iron*. DTU.
- Christensen, T. H., Bjerg, P. L., Banwart, S. A., Jakobsen, R., Heron, G., & Albrechtsen, H. J. (2000). Characterization of redox conditions in groundwater contaminant plumes. *Journal of Contaminant Hydrology*, 45(3–4), 165–241. [https://doi.org/10.1016/S0169-7722\(00\)00109-1](https://doi.org/10.1016/S0169-7722(00)00109-1)
- Christiansen, C. M., Damgaard, I., Broholm, M., Kessler, T., & Bjerg, P. L. (2012). Direct-push delivery of dye tracers for direct documentation of solute distribution in clay till. *Journal of Environmental Engineering*, 138(1), 27–37. [https://doi.org/10.1061/\(asce\)ee.1943-7870.0000451](https://doi.org/10.1061/(asce)ee.1943-7870.0000451)
- Christiansen, C. M., Damgaard, I., Broholm, M., Kessler, T., Klint, K. E., Nilsson, B., & Bjerg, P. L. (2010). Comparison of delivery methods for enhanced in situ remediation in clay till. *Groundwater Monitoring & Remediation*, 30(4), 107–122. <https://doi.org/10.1111/j.1745-6592.2010.01314.x>
- Ciampi, P., Esposito, C., Viotti, P., Boaga, J., Cassiani, G., & Petrangeli Papini, M. (2019). An integrated approach supporting remediation of an aquifer contaminated with chlorinated solvents by a combination of adsorption and biodegradation. *Applied Sciences*, 9(20), 4318. <https://doi.org/10.3390/app9204318>
- Cole, K. S., & Cole, R. H. (1941). Dispersion and absorption in dielectrics. I. Alternating current characteristics. *The Journal of Chemical Physics*, 9, 341–351. <https://doi.org/10.1063/1.1750906>
- Daily, W., & Ramirez, A. (1995). Electrical resistance tomography during in-situ trichloroethylene remediation at the Savannah River Site. *Journal of Applied Geophysics*, 33(4), 239–249. [https://doi.org/10.1016/0926-9851\(95\)90044-6](https://doi.org/10.1016/0926-9851(95)90044-6)
- Devlin, J. F. (2015). HydrogeoSieveXL: An excel-based tool to estimate hydraulic conductivity from grain-size analysis. *Hydrogeology Journal*, 23(4), 837–844. <https://doi.org/10.1007/s10040-015-1255-0>
- Fiandaca, G., Doetsch, J., Vignoli, G., & Auker, E. (2015). Generalized focusing of time-lapse changes with applications to direct current and time-domain induced polarization inversions. *Geophysical Journal International*, 203(2), 1101–1112. <https://doi.org/10.1093/gji/ggv350>
- Fiandaca, G., Madsen, L. M., & Maurya, P. K. (2018a). Re-parameterisations of the Cole-Cole model for improved spectral inversion of induced polarization data. *Near Surface Geophysics*, 16(4), 385–399.
- Fiandaca, G., Maurya, P. K., Balbarini, N., Hördt, A., Christiansen, A. V., Foged, N., et al. (2018b). Permeability estimation directly from logging-while-drilling Induced Polarization data. *Water Resources Research*, 54, 2851–2870. <https://doi.org/10.1002/2017WR022411>
- Fiandaca, G., Ramm, J., Binley, A., Gazoty, A., Christiansen, A. V., & Auker, E. (2013). Resolving spectral information from time domain induced polarization data through 2-D inversion. *Geophysical Journal International*, 192, 631–646. <https://doi.org/10.1093/gji/ggs060>
- Fjordbøge, A. S., Janniche, G. S., Jørgensen, T. H., Grosen, B., Wealthall, G., Christensen, A. G., et al. (2017). Integrity of clay till aquitards to DNAPL migration: Assessment using current and emerging characterization tools. *Groundwater Monitoring & Remediation*, 37(3), 45–61.
- Flores Orozco, A., Micić, V., Bückler, M., Gallistl, J., Hofmann, T., & Nguyen, F. (2019). Complex-conductivity monitoring to delineate aquifer pore clogging during nanoparticles injection. *Geophysical Journal International*, 218(3), 1838–1852. <https://doi.org/10.1093/gji/ggz255>
- Flores Orozco, A., Velimirovic, M., Tosco, T., Kemna, A., Sapion, H., Klaas, N., et al. (2015). Monitoring the injection of microscale zerovalent iron particles for groundwater remediation by means of complex electrical conductivity imaging. *Environmental Science & Technology*, 49(9), 5593–5600. <https://doi.org/10.1021/acs.est.5b00208>
- Grieger, K. D., Fjordbøge, A., Hartmann, N. B., Eriksson, E., Bjerg, P. L., & Baun, A. (2010). Environmental benefits and risks of zero-valent iron nanoparticles (nZVI) for in situ remediation: Risk mitigation or trade-off? *Journal of Contaminant Hydrology*, 118(3–4), 165–183. <https://doi.org/10.1016/j.jconhyd.2010.07.011>
- Hovedstaden, R. (2019). Notat. Hvedemarken 3-5, FARUM. Supplerende UNDERSØGELSER, FASE 1 OG FASE 2.
- Johnson, T., Versteeg, R. J., Day-Lewis, F. D., Major, W., & Lane, J. W., Jr. (2015). Time-lapse electrical geophysical monitoring of amendment-based biostimulation. *Groundwater*, 53(6), 920–932. <https://doi.org/10.1111/gwat.12291>
- Jørgensen, T. H., Scheutz, C., Durant, N. D., Cox, E., Rasmussen, P., & Bjerg, P. L. (2005). Stimuleret in situ reduktiv deklorering: Videnopsamling og screening af lokaliteter.
- Joyce, R. A., Glaser, D. R., II, Werkema, D. D., Jr., & Atekwana, E. A. (2012). Spectral induced polarization response to nanoparticles in a saturated sand matrix. *Journal of Applied Geophysics*, 77, 63–71. <https://doi.org/10.1016/j.jappgeo.2011.11.009>
- Kessler, T. C., Klint, K. E. S., Nilsson, B., & Bjerg, P. L. (2012). Characterization of sand lenses embedded in tills. *Quaternary Science Reviews*, 53(Suppl. C), 55–71. <https://doi.org/10.1016/j.quascirev.2012.08.011>
- LaBrecque, D. J., Ramirez, A. L., Daily, W. D., Binley, A. M., & Schima, S. A. (1996). ERT monitoring of environmental remediation processes. *Measurement Science and Technology*, 7(3), 375. <https://doi.org/10.1088/0957-0233/7/3/019>
- Lévy, L., Gibert, B., Sigmundsson, F., Flóvenz, Ó. G., Hersir, G. P., Briole, P., & Pezard, P. A. (2018). The role of smectites in the electrical conductivity of active hydrothermal systems: Electrical properties of core samples from Krafla volcano, Iceland. *Geophysical Journal International*, 215(3), 1558–1582.
- Lévy, L., Gibert, B., Sigmundsson, F., Parat, F., Deldicque, D., & Hersir, G. P. (2019a). Tracking magmatic hydrogen sulphur circulations using electrical impedance: Complex electrical properties of core samples at the Krafla volcano, Iceland. *Journal of Geophysical Research: Solid Earth*, 124, 2492–2509. <https://doi.org/10.1029/2018JB016814>
- Lévy, L., Maurya, P. K., Byrdina, S., Vandemeulebrouck, J., Sigmundsson, F., Arnason, K., et al. (2019b). Electrical resistivity tomography and time-domain induced polarization field investigations of geothermal areas at Krafla, Iceland: Comparison to borehole and laboratory frequency-domain electrical observations. *Geophysical Journal International*, 218(3), 1469–1489. <https://doi.org/10.1093/gji/ggz240>
- Martin, T., Titov, K., Tarasov, A., & Weller, A. (2021). Spectral induced polarization: Frequency domain versus time domain laboratory data. *Geophysical Journal International*, 225(3), 1982–2000. <https://doi.org/10.1093/gji/ggab071>
- Maurya, P. K., Balbarini, N., Møller, I., Rønne, V., Christiansen, A. V., Bjerg, P. L., et al. (2018). Subsurface imaging of water electrical conductivity, hydraulic permeability and lithology at contaminated sites by induced polarization. *Geophysical Journal International*, 213(2), 770–785. <https://doi.org/10.1093/gji/ggy018>
- Murray, A. M., Ottosen, C. B., Maillard, J., Holliger, C., Johansen, A., Brabæk, L., et al. (2019). Chlorinated ethene plume evolution after source thermal remediation: Determination of degradation rates and mechanisms. *Journal of Contaminant Hydrology*, 227, 103551. <https://doi.org/10.1016/j.jconhyd.2019.103551>
- Nazaroff, W. W., & Alvarez-Cohen, L. (2001). *Environmental engineering science*. John Wiley & Sons Inc.
- Nimmer, R. E., Osiensky, J. L., Binley, A. M., & Williams, B. C. (2008). Three-dimensional effects causing artifacts in two-dimensional, cross-borehole, electrical imaging. *Journal of Hydrology*, 359(1), 59–70. <https://doi.org/10.1016/j.jhydrol.2008.06.022>
- Nivorlis, A., Dahlin, T., Rossi, M., Höglund, N., & Sparrenbom, C. (2019). Multidisciplinary characterization of chlorinated solvents contamination and in-situ remediation with the use of the direct current resistivity and time-domain induced polarization tomography. *Geosciences*, 9(12), 487. <https://doi.org/10.3390/geosciences9120487>

- Nivorlis, A., Rossi, M., & Dahlin, T. (2021). Temporal filtering and time-lapse inversion of geoelectrical data for long-term monitoring with application to a chlorinated hydrocarbon contaminated site. *Geophysical Journal International*, 228(3), 1648–1664. <https://doi.org/10.1093/gji/ggab422>
- Olsen, J., Westergaard, A.-M., Laurbak, M. M., Pedersen, J. R., Poulsen, M. L., & Jespersen, K. (2020). Region's work with Earth pollution in 2019. In *Regionernes arbejde med jordforurening 2019—Fra indsigt til udsyn (in Danish)*. Danske Regioner.
- Olsson, P.-I., Fiandaca, G., Larsen, J. J., Dahlin, T., & Auken, E. (2016). Doubling the spectrum of time-domain induced polarization by harmonic de-noising, drift correction, spike removal, tapered gating and data uncertainty estimation. *Geophysical Journal International*, 207(2), 774–784. <https://doi.org/10.1093/gji/ggw260>
- Ottosen, C. B., Bjerg, P. L., Hunkeler, D., Zimmermann, J., Tuxen, N., Harrekilde, D., et al. (2021). Assessment of chlorinated ethenes degradation after field scale injection of activated carbon and bioamendments: Application of isotopic and microbial analyses. *Journal of Contaminant Hydrology*, 240, 103794. <https://doi.org/10.1016/j.jconhyd.2021.103794>
- Pelton, W. H., Ward, S. H., Hallof, P. G., Sill, W. R., & Nelson, P. H. (1978). Mineral discrimination and removal of inductive coupling with multifrequency IP. *Geophysics*, 43(3), 588–609. <https://doi.org/10.1190/1.1440839>
- Pérez, A. P., & Eugenio, N. R. (2018). *Status of local soil contamination in Europe*. Luxembourg: Publications Office of the European Union.
- Perri, M. T., Cassiani, G., Gervasio, I., Deiana, R., & Binley, A. (2012). A saline tracer test monitored via both surface and cross-borehole electrical resistivity tomography: Comparison of time-lapse results. *Journal of Applied Geophysics*, 79, 6–16. <https://doi.org/10.1016/j.jappgeo.2011.12.011>
- Phenrat, T., Kim, H.-J., Fagerlund, F., Illangasekare, T., Tilton, R. D., & Lowry, G. V. (2009). Particle size distribution, concentration, and magnetic attraction affect transport of polymer-modified Fe⁰ nanoparticles in sand columns. *Environmental Science & Technology*, 43(13), 5079–5085. <https://doi.org/10.1021/es900171v>
- Pridmore, D. F., & Shuey, R. T. (1976). The electrical resistivity of galena, pyrite, and chalcopyrite. *American Mineralogist*, 61(3–4), 248–259.
- Revil, A., Sleevi, M. F., & Mao, D. (2017). Induced polarization response of porous media with metallic particles—Part 5: Influence of the background polarization. *Geophysics*, 82(2), E77–E96. <https://doi.org/10.1190/geo2016-0388.1>
- Robinson, J., Johnson, T., & Slater, L. (2013). Evaluation of known-boundary and resistivity constraints for improving cross-borehole DC electrical resistivity imaging of discrete fractures. *Geophysics*, 78(3), D115–D127. <https://doi.org/10.1190/geo2012-0333.1>
- Robinson, J., Slater, L., Weller, A., Keating, K., Robinson, T., Rose, C., & Parker, B. (2018). On permeability prediction from complex conductivity measurements using polarization magnitude and relaxation time. *Water Resources Research*, 54, 3436–3452. <https://doi.org/10.1002/2017WR022034>
- Scheutz, C., Durant, N. D., Dennis, P., Hansen, M. H., Jørgensen, T., Jakobsen, R., et al. (2008). Concurrent ethene generation and growth of Dehalococcoides containing vinyl chloride reductive dehalogenase genes during an enhanced reductive dechlorination field demonstration. *Environmental Science & Technology*, 42(24), 9302–9309. <https://doi.org/10.1021/es800764t>
- Shi, Z., Fan, D., Johnson, R. L., Tratnyek, P. G., Nurmi, J. T., Wu, Y., & Williams, K. H. (2015). Methods for characterizing the fate and effects of nano zerovalent iron during groundwater remediation. *Journal of Contaminant Hydrology*, 181, 17–35. <https://doi.org/10.1016/j.jconhyd.2015.03.004>
- Shuey, R. T. (1975). *Semiconducting ore minerals*. Elsevier Scientific Publishing Company.
- Singha, K., Day-Lewis, F. D., Johnson, T., & Slater, L. D. (2015). Advances in interpretation of subsurface processes with time-lapse electrical imaging. *Hydrological Processes*, 29(6), 1549–1576. <https://doi.org/10.1002/hyp.10280>
- Singha, K., & Gorelick, S. M. (2005). Saline tracer visualized with three-dimensional electrical resistivity tomography: Field-scale spatial moment analysis. *Water Resources Research*, 41, W05023. <https://doi.org/10.1029/2004WR003460>
- Slater, L., Binley, A., Versteeg, R., Cassiani, G., Birken, R., & Sandberg, S. (2002). A 3D ERT study of solute transport in a large experimental tank. *Journal of Applied Geophysics*, 49(4), 211–229. [https://doi.org/10.1016/s0926-9851\(02\)00124-6](https://doi.org/10.1016/s0926-9851(02)00124-6)
- Slater, L., Binley, A. M., Daily, W., & Johnson, R. (2000). Cross-hole electrical imaging of a controlled saline tracer injection. *Journal of Applied Geophysics*, 44, 85–102. [https://doi.org/10.1016/s0926-9851\(00\)00002-1](https://doi.org/10.1016/s0926-9851(00)00002-1)
- Slater, L., Choi, J., & Wu, Y. (2005). Electrical properties of iron-sand columns: Implications for induced polarization investigation and performance monitoring of iron-wall barriers. *Geophysics*, 70(4), G87–G94. <https://doi.org/10.1190/1.1990218>
- Slater, L., Ntarlagiannis, D., & Wishart, D. (2006). On the relationship between induced polarization and surface area in metal-sand and clay-sand mixtures. *Geophysics*, 71(2), A1–A5. <https://doi.org/10.1190/1.2187707>
- Søndergaard, G. L., Binning, P. J., Bondgaard, M., & Bjerg, P. L. (2018). Multi-criteria assessment tool for sustainability appraisal of remediation alternatives for a contaminated site. *Journal of Soils and Sediments*, 18(11), 3334–3348.
- Stelman, C. M., Meyer, J. R., Wanner, P., Swanson, B. J., Conway-White, O., & Parker, B. L. (2020). The importance of transects for characterizing aged organic contaminant plumes in groundwater. *Journal of Contaminant Hydrology*, 235, 103728. <https://doi.org/10.1016/j.jconhyd.2020.103728>
- Stroo, H. F., & Ward, C. H. (2010). *In situ remediation of chlorinated solvent plumes*. Springer Science & Business Media.
- Sumner, J. S. (1976). *Principles of induced polarization for geophysical exploration*. In *Developments in economic geology* (Vol. 5). Elsevier Scientific Publishing Company.
- Switzer, A. D., & Pile, J. (2015). Grain size analysis. In *Handbook of sea-level research* (p. 331). <https://doi.org/10.1002/9781118452547.ch22>
- Thommerel, E., Valmalette, J. C., Musso, J., Villain, S., Gavarri, J. R., & Spada, D. (2002). Relations between microstructure, electrical percolation and corrosion in metal-insulator composites. *Materials Science and Engineering: A*, 328(1), 67–79. [https://doi.org/10.1016/s0921-5093\(01\)01680-x](https://doi.org/10.1016/s0921-5093(01)01680-x)
- Tsitonaki, A., Petri, B., Crimi, M., Mosbæk, H., Siegrist, R. L., & Bjerg, P. L. (2010). In situ chemical oxidation of contaminated soil and groundwater using persulfate: A review. *Critical Reviews in Environmental Science and Technology*, 40(1), 55–91. <https://doi.org/10.1080/10643380802039303>
- U.S. Environmental Protection Agency. (2017). Office of Land and Emergency Management (OLEM) accomplishments reports and benefits. Retrieved from <https://www.epa.gov/report%2Denvironment/contaminated%2Dland%23note1>
- Velimirovic, M., Tosco, T., Uytendaele, M., Luna, M., Gastone, F., De Boer, C., et al. (2014). Field assessment of guar gum stabilized microscale zerovalent iron particles for in-situ remediation of 1,1,1-trichloroethane. *Journal of Contaminant Hydrology*, 164, 88–99. <https://doi.org/10.1016/j.jconhyd.2014.05.009>
- Verardo, E., Atteia, O., Rouvreau, L., Siade, A., & Prommer, H. (2021). Identifying remedial solutions through optimal bioremediation design under real-world field conditions. *Journal of Contaminant Hydrology*, 237, 103751. <https://doi.org/10.1016/j.jconhyd.2020.103751>
- Vuković, M., & Soro, A. (1992). *Hydraulics of water wells: Theory and application*. Water Resources Publications.
- Waxman, M. H., & Smits, L. J. M. (1968). Electrical conductivities in oil-bearing shaly sands. *Society of Petroleum Engineers Journal*, 8, 107–122. <https://doi.org/10.2118/1863-a>

- Weller, A., & Slater, L. (2019). Permeability estimation from induced polarization: An evaluation of geophysical length scales using an effective hydraulic radius concept. *Near Surface Geophysics*, *17*(6), 581–594. <https://doi.org/10.1002/nsg.12071>
- Weller, A., Slater, L., Binley, A., Nordsiek, S., & Xu, S. (2015). Permeability prediction based on induced polarization: Insights from measurements on sandstone and unconsolidated samples spanning a wide permeability range. *Geophysics*, *80*(2), D161–D173. <https://doi.org/10.1190/geo2014-0368.1>
- Weller, A., Slater, L., & Nordsiek, S. (2013). On the relationship between induced polarization and surface conductivity: Implications for petrophysical interpretation of electrical measurements. *Geophysics*, *78*(5), D315–D325. <https://doi.org/10.1190/geo2013-0076.1>
- Wilkinson, P. B., Chambers, J. E., Lelliott, M., Wealthall, G. P., & Ogilvy, R. D. (2008). Extreme sensitivity of crosshole electrical resistivity tomography measurements to geometric errors. *Geophysical Journal International*, *173*(1), 49–62. <https://doi.org/10.1111/j.1365-246x.2008.03725.x>
- Wilkinson, P. B., Meldrum, P. I., Kuras, O., Chambers, J. E., Holyoake, S. J., & Ogilvy, R. D. (2010). High-resolution electrical resistivity tomography monitoring of a tracer test in a confined aquifer. *Journal of Applied Geophysics*, *70*(4), 268–276. <https://doi.org/10.1016/j.jappgeo.2009.08.001>
- Xin, J., Zheng, X., Han, J., Shao, H., & Kolditz, O. (2015). Remediation of trichloroethylene by xanthan gum-coated microscale zero valent iron (XG-mZVI) in groundwater: Effects of geochemical constituents. *Chemical Engineering Journal*, *271*, 164–172. <https://doi.org/10.1016/j.cej.2015.02.092>